

Investigating the physical properties of dusty star-forming galaxies at $z \gtrsim 1.5$ in the GOODS-South field using JWST

DIPANJAN MITRA,¹ MATTIA NEGRELLO,¹ AND GIANFRANCO DE ZOTTI²

¹*School of Physics and Astronomy, Cardiff University, The Parade, CF24 3AA, UK*

²*INAF, Osservatorio Astronomico di Padova, Vicolo Osservatorio 5, I-35122, Padova, Italy*

ABSTRACT

We investigated how well the physical properties of progenitors of present-day massive spheroidal galaxies (proto-spheroids) can be constrained by the *JWST* Advanced Deep Extragalactic Survey (JADES) in the GOODS-South field, which benefits from extensive photometric and spectroscopic data, including those from the *Hubble*, *Spitzer* and *Herschel*. We adopted a physical model for the evolution of proto-spheroidal galaxies, which form the bulk of dusty star-forming galaxies (DSFGs) at $z \gtrsim 1.5$ and confirmed its consistency with recent mid-infrared high- z galaxy luminosity functions. Using the model and the JADES survey strategy, we simulated a sample of proto-spheroids over 87.5 arcmin², matching the JADES/GOODS-S survey area. Photometric redshifts estimated from simulated *JWST* photometry showed $\gtrsim 95\%$ accuracy and were used in SED fitting with CIGALE. We demonstrated that *JWST* will provide reliable stellar mass estimates up to 0.1 dex for the majority of proto-spheroids at $z \gtrsim 1.5$ and can detect low-mass systems during cosmic noon that were inaccessible in the pre-*JWST* era. Focusing on the active star-forming phase of the proto-spheroid evolution, we defined a sub-sample flux limited at 250 μ m (DSFG sample) and derived SFR, dust luminosity and dust mass complementing the *JWST* photometry with that from *Spitzer*/MIPS and *Herschel*. We also constructed a *JWST*-selected DSFG catalog from ASTRODEEP data using NIRCcam colour criteria and demonstrated strong consistency between the observed and simulated DSFG populations.

1. INTRODUCTION

The discovery of dusty star-forming galaxies (DSFGs), also known as sub-millimetre galaxies (SMGs; [I. Smail et al. 1997](#); [A. J. Barger et al. 1998](#); [D. H. Hughes et al. 1998](#)) revolutionised our understanding of galaxy evolution and the study of these high- z dusty sources became a crucial area of extragalactic astronomy. It is now widely agreed, based on several observational evidences, that high- z SMGs can be interpreted as being the progenitors of present-day massive spheroidal galaxies ([S. J. Lilly et al. 1999](#); [A. M. Swinbank et al. 2006](#); [L. J. Hainline et al. 2011](#); [S. Toft et al. 2014](#); [J. M. Simpson et al. 2014, 2017](#); [C.-L. Liao et al. 2024](#); [Q.-H. Tan et al. 2024](#); [J. E. Birkin et al. 2024](#); [A. Amvrosiadis et al. 2025](#)); in the following, these will be referred to as proto-spheroidal galaxies or proto-spheroids. This interpretation is consistent with the relatively old ages of stellar populations of nearby early-type galaxies ([D. Thomas et al. 2010](#); [M. Bernardi et al. 2010](#); [S. Lu et al. 2023](#)), implying that these galaxies formed the bulk of their stars at early times ($\log(\text{age}/\text{yr}) \gtrsim 9.5$ correspond-

ing to $z \gtrsim 1.5$), on a relatively short timescale, with high SFRs, and were quenched afterwards.

The fact that SMGs are frequently found to be gas-rich rotation-dominated disks (e.g., [B. Gullberg et al. 2019](#); [S. Gillman et al. 2023](#)) is not in conflict with this interpretation. The extensive analysis of ALMA sub-millimeter surface brightness profiles of SMGs by [Q.-H. Tan et al. \(2024\)](#) has highlighted that most of these galaxies are fully triaxial rather than flat disks. Other studies have pointed out that disk SMGs are dynamically hotter than local disc galaxies (i.e., have lower ratios of rotation to random velocity) and with a larger fraction of irregular morphologies ([F. Lelli et al. 2016](#); [A. M. Swinbank et al. 2017](#); [O. J. Turner et al. 2017](#); [E. Wisnioski et al. 2019](#); [N. M. Förster Schreiber & S. Wuyts 2020](#); [J. S. Kartaltepe et al. 2023](#); [J. E. Birkin et al. 2024](#)).

The pathway from SMGs to evolved spheroidal galaxies, implying kinematic and morphological evolution, is, however, still not completely clear. In our reference scenario ([G. L. Granato et al. 2004](#); [Z.-Y. Cai et al. 2013](#); [A. Lapi et al. 2014](#)), high- z SMGs evolve to the galaxy main sequence, with lower dust-to-stellar-mass ratios and substantially lower specific SFR compared to SMGs

(C. Mancuso et al. 2016), and end in passive evolution. In this process their stellar mass grows while their dust obscuration decreases as a result of supernova and AGN feedback, which sweep off the interstellar medium.

So far, the observational assessment of the evolutionary history of spheroidal galaxies has been hampered to limited depth and poor angular resolution of the instruments. The next generation instruments already launched like the *James Webb Space Telescope* (*JWST*; J. P. Gardner et al. 2006; J. Rigby et al. 2023; M. W. McElwain et al. 2023), the *Euclid* space observatory (R. Laureijs et al. 2011) and those in preparation like the *Vera C. Rubin Legacy Survey of Space and Time* (*LSST*; . Ivezi et al. 2019) will be able to overcome the above limitations with unprecedented sensitivity and resolution.

In this paper we investigate the potential of the *JWST* Advanced Deep Extragalactic Survey (JADES; D. J. Eisenstein et al. 2023) for shedding light on the proto-spheroid evolution. We adopt the standard approach, exploiting models to simulate the survey outcome. A phenomenological model specifically designed to simulate *JWST* extragalactic surveys was presented by C. C. Williams et al. (2018) who applied it to make predictions for the JADES in GOODS-South and GOODS-North fields (M. Giavalisco et al. 2004), aiding their optimization and the interpretation of the data. These fields are among the best-studied extragalactic deep fields with the availability of a large amount of photometric and spectroscopic data from the ultraviolet to the far-infrared, including data from the Hubble Space Telescope (*HST*), *Spitzer*, and *Herschel* (D. Liu et al. 2018; G. Barro et al. 2019).

In this paper we exploit the model by Z.-Y. Cai et al. (2013) which co-evolves massive proto-spheroids and the central AGN at $z \gtrsim 1.5$. It is a physical model, therefore well suited to link the observational data to the physics driving the early galaxy evolution. Importantly, the model captures the full life-cycle of massive galaxies: starting with an initial UV-bright star-forming phase, followed by a heavily dust-enshrouded starburst phase (corresponding to the DSFG stage), then transitioning through a short-lived quasar phase, before settling into passive evolution.

We adopt the version upgraded by D. Mitra et al. (2024), which links the model outputs to the formalism by E. da Cunha et al. (2008) and by J. Fritz et al. (2006) to compute the spectral energy distributions (SEDs) of DSFG and of AGN components, respectively. The model was used by D. Mitra et al. (2024) to study the ability of *Euclid* in constraining the physical properties of DSFGs at $z \gtrsim 1.5$ detected by the *Herschel* Astro-

physical Terahertz Large Area Survey (H-ATLAS; S. Eales et al. 2010).

In the pre-*JWST* era, several studies have been conducted to estimate the physical properties of DSFGs in the GOODS-S field. M. Franco et al. (2020) studied a sample of 35 galaxies detected with *ALMA* at 1.1 mm in the GOODS-*ALMA* field (M. Franco et al. 2018). To derive their physical properties, they performed SED fitting using the available multi-wavelength data. The sample comprised massive galaxies having a median stellar mass estimate of $8.5 \times 10^{10} M_{\odot}$ in the redshift range $z \sim 2 - 4$. Y. Yamaguchi et al. (2020) estimated the physical properties of a sample of 24 K-band selected galaxies from the Four Star Galaxy Evolution Survey (ZFOURGE; C. M. S. Straatman et al. 2016) having deep 1.2 mm *ALMA* observations, as a part of the *ALMA* twenty-six Arc minute² Survey of GOODS-S at One-millimeter (ASAGO)³. With a median redshift of 2.38 ± 0.14 , these sources have median stellar mass estimates of $\log(M_{\star}/M_{\odot}) \sim 10.75$ in both the redshift bins $1 < z \leq 2$ and $2 < z \leq 3$. In the same redshift bins, the obtained median $\log(\dot{M}_{\star}/M_{\odot}\text{yr}^{-1})$ were 2.14 and 2.15, respectively. T. Wiklind et al. (2014) studied a sample of 10 sub-mm sources observed with *ALMA* at 870 μm originally detected using *LABOCA* (G. Siringo et al. 2009) in the CANDELS survey of the GOODS-S. A median stellar mass estimate of $9.1 \times 10^{10} M_{\odot}$ was obtained. The average SFR obtained was $(0.8 \pm 0.7) \times 10^3 M_{\odot}\text{yr}^{-1}$. A panchromatic study of 11 DSFGs with spectroscopic redshift $1.5 < z_{\text{spec}} < 3$ in the GOODS-S field was conducted by L. Pantoni et al. (2021). They performed SED fitting using CIGALE and estimated the median stellar mass and SFR of the sources to be $6.5 \times 10^{10} M_{\odot}$ and $241 M_{\odot}\text{yr}^{-1}$, respectively. As can be seen, the studies conducted so far on DSFGs in the GOODS-S could only probe median stellar masses down to about $\log(M_{\star}/M_{\odot}) \approx 10.8$. In this work, we also try to investigate the minimum stellar mass at which *JWST* can reliably detect DSFGs.

The paper is organised as follows. Section 2 gives a brief description of the model. In Section 3, we provide a concise presentation of the relevant surveys. Section 4 presents a comparison of physical properties of ASTRODEEP-*JWST* sources with model predictions. Finally, Section 5 contains the summary and the conclusions of this paper. Here, we adopt a flat Λ -CDM cosmology with present-day matter density (in units of the critical density), $\Omega_{m,0} = 0.3153$ and baryon density $\Omega_{b,0} = 0.0493$. We set the value of the Hubble-Lemaître

³ <https://sites.google.com/view/asago26/home>

constant to $h = H_0/100 = 0.6736$, the slope of the spectrum of primordial density perturbations to $n = 0.9649$ and the normalization of the density fluctuations on a scale of $8h^{-1}$ Mpc to $\sigma_8 = 0.8111$ (Planck Collaboration VI, 2020).

2. METHODOLOGY

2.1. Model Outline

The Z.-Y. Cai et al. (2013) model was inspired by the fact that the stellar content of present-day massive spheroidal galaxies is dominated by old populations, formed at $z \gtrsim 1.5$. In contrast, the disc-shaped galaxies contain relatively young stellar populations, with luminosity-weighted age $\lesssim 7$ Gyr, i.e. mostly formed at $z \lesssim 1$. Therefore, at $z \gtrsim 1.5$, the dominant star-forming galaxies are the proto-spheroidal galaxies, the progenitors of the present-day ellipticals. This physical treatment takes into account the co-evolution of the SFR of the proto-spheroids and of the supermassive black holes (SMBHs) residing at their centre.

The star formation history of these proto-spheroids is determined by a set of equations that describe the gas cooling and condensation into stars, the accretion of the gas into the SMBH as well as the feedback from the supernova explosions and from the AGN. We refer the readers to Z.-Y. Cai et al. (2013) and D. Mitra et al. (2024) for more detailed explanations about the equations governing the co-evolution of the stellar and of the AGN components.

The SED of the photo-spheroids is modelled using the formalism put forward by E. da Cunha et al. (2008) which is based on the principle of energy balance, with a few modifications explained in detail in D. Mitra et al. (2024). We adopt the smooth torus model introduced by J. Fritz et al. (2006) to model the SED of the AGN component. In modelling the dust emission from the AGN, we do not incorporate the contribution from polar dust (S. F. Hnig et al. 2013; Q. Yang et al. 2020) as it emits mostly in the mid-IR and has a negligible effect at UV/optical/near-IR wavelengths (S. F. Hnig et al. 2013, see their Figure 8).

To verify that this modified version of Cai’s model correctly predicts the luminosity functions (LFs) of proto-spheroidal galaxies at mid-IR wavelengths, we computed the rest-frame LFs of these galaxies at 7.7, 10, 12.8, 15, 18 and 21 μm respectively, and compared them with the rest-frame LFs produced by C.-T. Ling et al. (2024) using a sample of 506 galaxies at $z = 0 - 5.1$ from the *JWST* Cosmic Evolution Early Release Science (CEERS; S. L. Finkelstein et al. 2017) survey. Figure 1 shows the plot of the mid-IR LFs for redshift $z = 1.8, 2.5$ and 3.5 respectively.

It is to be noted that the values of model parameters are not optimized, i.e. no fit of the data was attempted. The model curve (red) shows the contribution of galaxies with virialized halo masses in the range $11.3 \leq \log(M_{\text{vir}}/M_{\odot}) \leq 13.3$ (see D. Mitra et al. 2024, and sub-Sect. 2.3). The adopted lower limit to halo masses translates to a fast decrease of the model LFs at low luminosities, where less massive galaxies dominate. As a consequence, the model under-predicts the low-luminosity end of LFs. Decreasing the minimum halo mass would make the model predictions less solid. This is because a basic assumption of the model, namely that the halo formation rate is well approximated by the positive term of the cosmic time derivative of the halo mass function, is less accurate at low halo masses.

At high luminosity, the consistency with observations is satisfactory, especially considering that the model is not optimized. At some combinations of rest-frame wavelength and redshift, the complexity of the SED at MIR wavelengths, where the PAH features are prominent, can also contribute, to the small discrepancy between the predicted and the measured luminosity functions. In fact, such a complexity is not fully captured by our formalism, which adopts only a single template for the PAHs.

2.2. NIRCam colour comparison between CEERS and the model

To further evaluate the realism of our simulated proto-spheroidal galaxies, we compare their near-infrared colours to galaxies observed in the CEERS survey using a $F150W - F277W$ vs. $F277W - F444W$ colour-colour diagram as shown in Figure 2. The CEERS sources, shown in grey, are taken from the ASTRODEEP-*JWST* catalog (E. Merlin et al. 2024, for more details see Section 4.3) and span a broad range of redshifts, dust contents, and stellar populations, forming a wide distribution in the colour-colour plane. In contrast, the simulated proto-spheroids (cyan points), occupy a more confined region. Notably, these galaxies follow a trend consistent with high-redshift star-forming systems, with moderate to substantial dust obscuration. Overlaid on the plot are evolutionary tracks of dusty galaxies based on V-band dust attenuation (A_V) and redshifted from $z = 1$ to 6 by A. S. Long et al. (2024). These tracks illustrate how dust attenuation and redshift drive the observed colours. The lower, middle, and upper tracks correspond to $A_V < 1$ (little attenuation, $A_V \sim 2$ (average attenuation), and $A_V \gtrsim 3$ (high attenuation), respectively. They obtain these evolutionary tracks using the SEDs of ALESS submillimeter galaxies from E. da Cunha et al. (2015). The majority of the simulated

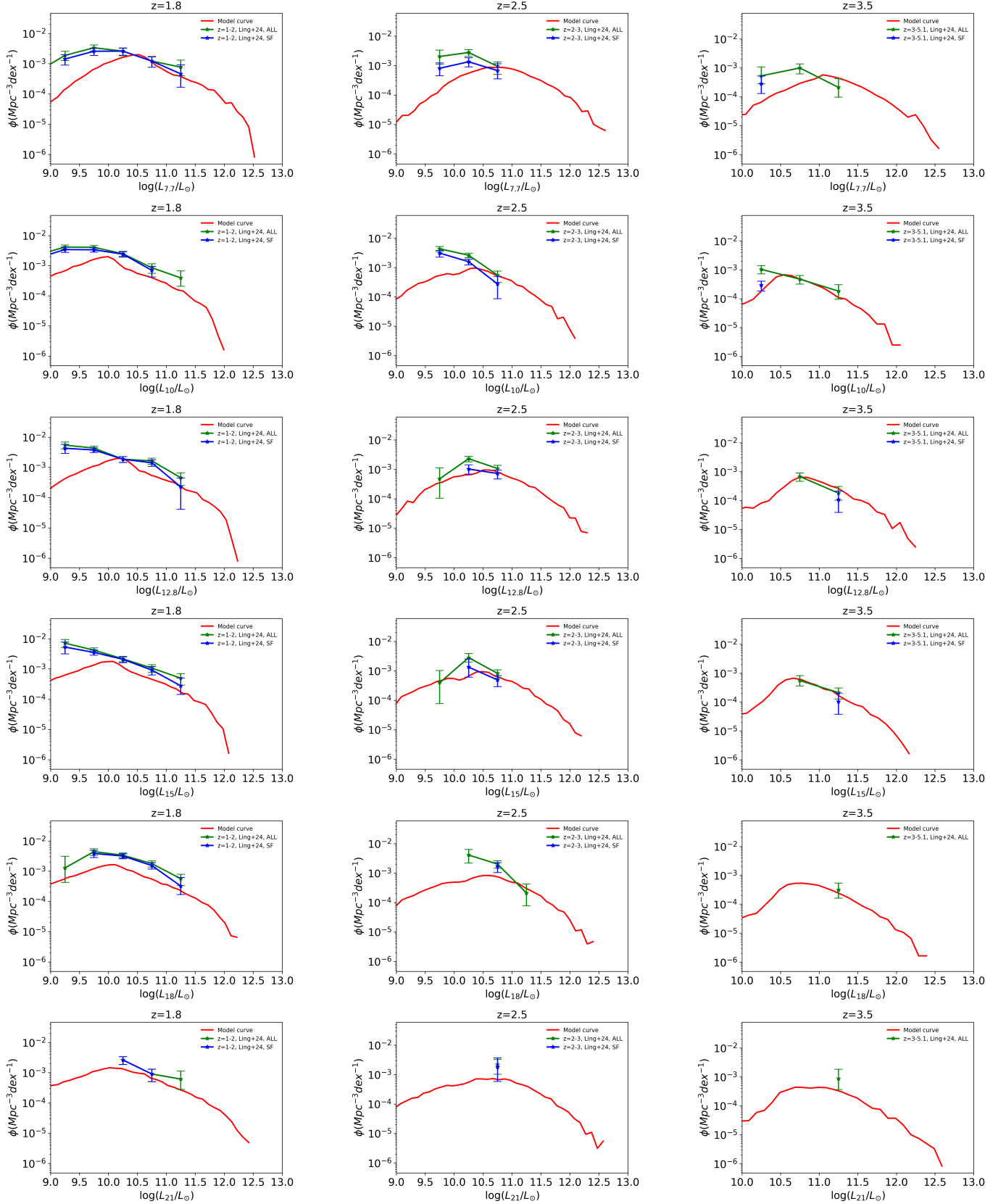


Figure 1. Comparison of the measured monochromatic LFs with those predicted for the population of massive ($11.3 \leq \log(M_{\text{vir}}/M_{\odot}) \leq 13.3$) proto-spheroids at 7.7, 10, 12.8, 15, 18, and 21 μm for $z = 1.8$, 2.5, and 3.5. The red line shows the model curve. Note that the model parameters were not optimized; no fit of the data was attempted. At low luminosity the dominant contribution to the LFs comes from galaxies with halo masses below the adopted lower limit. This leads to a fast decrease of the model curve at low luminosity, implying an under-prediction of the LFs. The green line shows the LF from C.-T. Ling et al. (2024) for all galaxy populations, while the blue line shows the same for the star-forming (SF) galaxies. The first column shows the data points for the redshift bin $z = 1 - 2$, the middle column for $z = 2 - 3$, and the last column for $z = 3 - 5.1$.

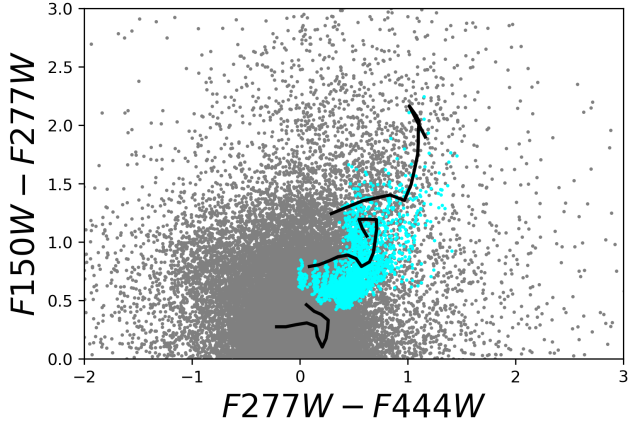


Figure 2. *JWST*/NIRCam $F150W - F277W$ versus $F277W - F444W$ colour-colour diagram. Grey points represent observed galaxies from the CEERS survey (taken from the ASTRODEEP-*JWST* catalog), and cyan points show simulated proto-spheroids from our model. The black curves represent evolutionary tracks from redshift $z \sim 1$ to 6 for galaxies with different dust attenuations: $A_V < 1$ (bottom), $A_V \sim 2$ (middle), and $A_V \gtrsim 3$ (top). The model galaxies align well with the moderately to heavily obscured tracks, indicating a good consistency between simulated and observed colour distributions.

DSFGs cluster at moderate attenuation, consistent with the expected properties of proto-spheroids at $z \gtrsim 1.5$.

2.3. Building the Simulated Catalogue

Here we give a brief explanation about the generation of a simulated sample of proto-spheroidal galaxies to be used for forecast and analysis. The building of the simulated catalogue starts by randomly sampling the formation rate function of dark matter haloes (see Eq. (A25) of D. Mitra et al. 2024) in both the virialisation mass (M_{vir}) and the virialisation redshift (z_{vir}) of the halos. We restrict ourselves to the ranges $11.3 \leq \log(M_{\text{vir}}/M_{\odot}) \leq 13.3$ and $1.5 \leq z_{\text{vir}} \leq 8$ respectively.

The number of sampled halos depends on the size of the surveyed area of the sky. Here we consider a survey area of 87 square arcmin., like that covered by the JADES-Medium survey in the GOODS-S field. We then allow the baryons within the simulated halos to evolve into galaxies by solving the equations of the model by Z.-Y. Cai et al. (2013) to get the star formation history (SFH) and the black hole accretion rate (BHAR) as a function of the galaxy age. The galaxy is assumed to be born at z_{vir} . Next, we generate the SEDs of both the stellar and the AGN components of simulated galaxies. We refer the readers to D. Mitra et al. (2024) for a detailed description of the steps involved and of the adopted values of the different parameters.

3. FORECASTS

Here, we investigate to what extent *JWST* can constrain the physical properties of high- z proto-spheroids along with the minimum stellar mass at which *JWST* can reliably detect them in the GOODS-S field, the primary JADES field. Since the CANDELS survey studied the GOODS-S field using *HST*, we also complement the *JWST* data with the *HST* data. IR and sub-mm data from *Spitzer* and *Herschel* are also available for this field. We examine the effect on the physical parameters by considering different combinations of data from UV to IR/sub-mm with *JWST* photometry from JADES. To begin with, we provide a brief summary of the CANDELS and of the JADES survey programs and then proceed with the results and the analysis.

3.1. A brief overview of the CANDELS and JADES survey

The Cosmic Assembly Near-infrared Deep Extragalactic Legacy Survey (CANDELS; N. A. Grogin et al. 2011; A. M. Koekemoer et al. 2011) was designed to study galaxy formation and evolution over the $1.5 \leq z \leq 8$ range. The main idea behind it was to exploit the revolutionary NIR *HST*/WFC3 camera for obtaining deep imaging of distinct faint objects. Parallel observations using *HST*/ACS were also carried out, to provide multi-wavelength coverage of galaxies. The survey covered 800 sq. arcmin. of the sky in five fields: GOODS (both North and South; M. Giavalisco et al. 2004), UDS (A. Lawrence et al. 2007), EGS (M. Davis et al. 2007), and COSMOS (N. Scoville et al. 2007). The *HST* filters used in CANDELS are F435W, F606W, F775W, F814W, and F850LP for *HST*/ACS; and F098M, F105W, F125W, and F160W filters for *HST*/WFC3. Table 1 gives the 5σ point source sensitivity values of the *HST* filters used, from Y. Guo et al. (2013). The CANDELS/GOODS survey also has mid-/far-IR observations from *Spitzer* (MIPS - 24 μm , 70 μm) and *Herschel* (PACS - 100 μm , 160 μm , SPIRE - 250 μm , 350 μm and 500 μm). The table also provides the 5σ limits for the FIR filters, from G. Barro et al. (2019).

The *JWST* Advanced Deep Extragalactic Survey (JADES; D. J. Eisenstein et al. 2023) is a joint project of the NIRCam (M. J. Rieke et al. 2023) and NIRSpec (P. Jakobsen et al. 2022) Instrument Development teams. JADES is the largest program being conducted in the Cycle 1 run of *JWST* with an observing time of 770 hours; it observes two of the best-studied deep fields, namely GOODS-South and GOODS-North. The main focus is on GOODS-S, which includes the *Chandra* Deep Field South (R. Giacconi et al. 2002) and the *Hubble* Ultra Deep field (S. V. W. Beckwith et al. 2006). Along

with that, deep *ALMA* (M. Franco et al. 2018; B. Hatsukade et al. 2018) and *JVLA* data (S. Alberts et al. 2020) are available for this field. The GOODS-N, which contains the Hubble deep field and was covered by a deep Chandra survey, was chosen as the second field.

The design of JADES is like a two-layer wedding cake comprising deep portions of both imaging and spectroscopic data, along with medium-depth surveys over larger areas. The continuous portions of NIRC*am* imaging are named as “prime” while those with parallel NIR-Spec exposures are designated as “parallel”. JADES-Deep comprises a survey area of 36 sq. arcmin. while JADES-Medium covers 175 sq. arcmin.. The JADES-Deep survey will be carried out only on GOODS-S. The survey area of JADES-Medium is almost equally distributed between the GOODS-N and the GOODS-S fields. NIRC*am* imaging in JADES is done using nine filters namely F090W, F115W, F150W, F200W, F277W, F335M, F356W, F410M and F444W. The mean wavelength and the 5σ depth for each filter are given in Table 1.

3.2. Simulation set-up

A source in the simulated catalogue is said to be detected by *JWST* if its flux density is $> 5\sigma$ in all the NIRC*am* bands. To incorporate *HST* photometry, we apply the 5σ detection criteria to ACS/F435W and WFC3/F160W filters on *JWST* detected sources. For *Herschel* we adopt the 5σ detection limit in the SPIRE 250 μm band. Among these sources, we say a source is detected by *Spitzer*/MIPS if it has a flux density $> 5\sigma$ at both 24 μm and 70 μm .

To investigate the detectability of proto-spheroids by *JWST*, we have simulated galaxies having virialised halo mass in the range $11.3 \leq \log(M_{\text{vir}}/M_{\odot}) \leq 13.3$. We call this the “parent sample”; it comprises 27748 galaxies detected at 5σ in all the 9 NIRC*am* bands. Approximately 41% of them are also detected by *HST* above 5σ in the F435W and F160W bands. However, only 1.5% and 1.7% of these *JWST* sources are detected above 5σ by *Spitzer* and *Herschel* respectively. While *JWST* can help to constrain the stellar mass of galaxies, FIR observations are crucial in constraining the SFR of DSFGs.

To get a larger fraction of detections by *Herschel* and *Spitzer*, we simulated all galaxies with $12 \leq \log(M_{\text{vir}}/M_{\odot}) \leq 13.3$; galaxies with $\log(M_{\text{vir}}/M_{\odot}) < 12$ are undetected by *Herschel*. In this sub-sample there are 507 galaxies above the *Herschel* 5σ detection limit at 250 μm ; these constitute our DSFG sample. Among them, 503 galaxies, approximately 99%, are detected at 5σ in all the 9 NIRC*am* bands. *HST* detects $\approx 98.8\%$

Table 1. *HST*, *JWST*, *Spitzer* and *Herschel* filters along with their central wavelengths and 5σ depths (5σ depths are in AB magnitudes except for *Spitzer* and *Herschel*). The *JWST* limiting magnitudes refer to JADES-Medium.

Filter	Central Wavelength (μm)	5σ depth
F435W/ACS/ <i>HST</i>	0.436	28.95
F606W/ACS/ <i>HST</i>	0.603	29.35
F775W/ACS/ <i>HST</i>	0.773	28.55
F814W/ACS/ <i>HST</i>	0.813	28.84
F850LP/ACS/ <i>HST</i>	0.908	28.55
F098M/WFC3/ <i>HST</i>	0.990	28.77
F105W/WFC3/ <i>HST</i>	1.065	28.45
F125W/WFC3/ <i>HST</i>	1.257	28.34
F160W/WFC3/ <i>HST</i>	1.543	28.16
F090W/NIRC <i>am</i> / <i>JWST</i>	0.98	28.85
F115W/NIRC <i>am</i> / <i>JWST</i>	1.162	28.98
F150W/NIRC <i>am</i> / <i>JWST</i>	1.510	28.93
F200W/NIRC <i>am</i> / <i>JWST</i>	2.002	29.02
F277W/NIRC <i>am</i> / <i>JWST</i>	2.784	29.32
F335M/NIRC <i>am</i> / <i>JWST</i>	3.367	28.89
F356W/NIRC <i>am</i> / <i>JWST</i>	3.593	29.32
F410M/NIRC <i>am</i> / <i>JWST</i>	4.088	28.87
F444W/NIRC <i>am</i> / <i>JWST</i>	4.439	29.03
<i>Spitzer</i> /MIPS	24	0.03 mJy
<i>Spitzer</i> /MIPS	70	2.5 mJy
<i>Herschel</i> /PACS	100	1.1 mJy
<i>Herschel</i> /PACS	160	3.4 mJy
<i>Herschel</i> /SPIRE	250	8.3 mJy
<i>Herschel</i> /SPIRE	350	11.5 mJy
<i>Herschel</i> /SPIRE	500	11.3 mJy

of these DSFGs, while 434 ($\approx 86\%$) are detected in both *Spitzer*/MIPS bands at $> 5\sigma$.

3.3. Estimation of Photometric Redshifts and Galaxy Physical Properties

To estimate the physical properties of galaxies, the knowledge of redshift is essential. Therefore, the first thing that we estimated for our simulated sample was the redshift from the *JWST* photometry. Since the *HST* photometry is available for most of the sources, we also estimated the photometric redshift by complementing the *JWST* photometry with that from *HST*.

We used the template-based photo- z estimation code EAZY (Easy and Accurate Redshifts from Yale; G. B. Brammer et al. 2008). This code is applicable for the estimation of photo- z using UV/optical/near-IR photometric data. We use “v1.3” of EAZY which uses 9 templates. The original 5 templates of “v1.0” of EAZY are

from A. Grazian et al. (2006). The dusty galaxies are taken into account by adding a starburst template with $t = 50$ Myr and $A_V = 2.75$. The evolved simple stellar population (SSP) model by C. Maraston (2005) is added to include massive old galaxies at $z < 1$. The dust template is taken from D. K. Erb et al. (2010). The P. Madau (1995) model for dust absorption by the intergalactic medium (IGM) is also taken into account in EAZY. A redshift range of $z = 1$ to 8 in steps of $\Delta z = 0.01$ was chosen.

After estimating the photo- z , we proceeded to estimate the physical properties of the simulated galaxies. For this, we used the SED fitting code CIGALE (Code Investigating GALaxy Emission; D. Burgarella et al. 2005; S. Noll et al. 2009; M. Boquien et al. 2019) which uses the principle of “energy balance” i.e., the amount of stellar energy absorbed by dust in the UV/optical regime is entirely processed and re-emitted at far-IR/sub-mm wavelengths, to build the panchromatic model of the SEDs of galaxies. The SED templates generated by CIGALE depend on the modules and values of different parameters chosen by the user. In this work, we adopted a delayed SFH with an additional late burst of star formation. The G. Bruzual & S. Charlot (2003) SSP models along with a Chabrier initial mass function (IMF; G. Chabrier 2003) and solar metallicity are chosen. The S. Charlot & S. M. Fall (2000) model is used for modelling the dust attenuation. The dust emission is modelled following B. T. Draine et al. (2014). To incorporate the contribution from the AGN, templates from J. Fritz et al. (2006) are used. With the above-chosen modules and parameter values (see Table 2), CIGALE generated around 6 billion SED templates and then used a χ^2 minimisation technique to get the best fit SED and estimate the physical properties (S. Noll et al. 2009).

4. RESULTS

In this section, we discuss the results obtained for the photometric redshifts and for the physical properties of the *JWST*-detected simulated galaxies.

4.1. Derived photometric redshift

The scatter plot of the photometric redshifts estimated from the *JWST* photometry alone versus the input redshifts is shown in the left-hand panel of Figure 3 for both the parent catalogue (top panel) and the DSFG sub-sample (bottom panel) of galaxies. We observe that *JWST* provides a good redshift estimate up to $z \sim 4$ for both the parent sample and the sub-sample. The outlier fraction, defined as $|\Delta z|/(1 + z_{\text{input}}) > 0.15$ where $|\Delta z| = |z_{\text{input}} - z_{\text{phot}}^{\text{EAZY}}|$ (C. Laigle et al. 2016), is

$f_{\text{outlier}} = 0.05$ for the parent sample and $f_{\text{outlier}} = 0.042$ for the DSFG sub-sample respectively. The most catastrophic errors on z occur in the range $4 \leq z \leq 5 - 6$, where there is a leakage of high- z sources to the low redshift regime. Also, a few galaxies at $z \sim 2$ are wrongly assigned a redshift $z > 4$. These wrong estimations of redshift are mostly due to the degeneracy between the Lyman- α break at 912 and the 4000 break. The right-hand panels of Figure 3 show the estimated versus true photo- z values for the *JWST* sources which are also detected by *HST*. We observe that, on complementing the *JWST* photometry with that from *HST*, most of the low- z contaminants are removed and we get a very good level of agreement between the input and the estimated photo- z values at all redshifts up to $z \leq 5$. Thanks to the availability of the *HST* photometry, EAZY can properly sample the Lyman break and the degeneracy with the 4000 break is rectified. This is because, at $z \sim 4 - 5$, the Lyman break is missed by the *JWST* NIRCcam filters, but it falls within the *HST* filters. However, for the parent sample, there are still some catastrophic redshift determinations. These are mostly AGN-dominated sources, the SEDs of which are featureless and power-law shaped, which makes it difficult for EAZY to give a correct estimation of redshift. The outlier fraction, for the *JWST*+*HST* photometry, is reduced to $f_{\text{outlier}} = 0.019$ and $f_{\text{outlier}} = 0.008$ for the parent sample and the DSFG sub-sample, respectively. Overall, the recovery of redshifts for DSFGs using *JWST* photometry demonstrates excellent performance, with high accuracy and remarkably low outlier fractions. The broad wavelength coverage and the high sensitivity of NIRCcam enable reliable photometric redshift estimates even for heavily dust-obscured systems. This highlights *JWST*’s unique capability to precisely constrain the redshift distribution of DSFGs, which has been a major challenge for previous infrared and optical surveys.

For the DSFG sample, we attempted to estimate photometric redshifts using *Herschel*/SPIRE photometry based on the E. A. Pearson et al. (2013) template set. However, this approach resulted in a high outlier fraction of approximately 33%. Even after restricting the analysis to sources with additional 5σ detections at both 350 and 500 μm , the outlier fraction remained high, at 28%. Due to this significant level of inaccuracy, we do not adopt the FIR-based redshift estimates in our analysis. Instead, we rely on photometric redshifts estimated using EAZY applied to *JWST* photometry for the rest of our analysis.

Table 2. Parameter values given as input to CIGALE for SED fitting

SFH : sfhdelayed - delayed SFH with optional exponential burst	
e-folding time of the main stellar population (Myr)	500, 1000, 2000, 3000, 4000, 5000, 6000, 7000
e-folding time of the late starburst population (Myr)	1000, 5000, 10000
mass fraction of the late starburst population	0.0, 0.001, 0.01, 0.1, 0.15, 0.3, 0.5
age of the main stellar population (Myr)	500, 1000, 2000, 3000, 5000, 6000, 7000, 8000, 9000, 10000
age of the late starburst (Myr)	10, 30, 50, 70, 100, 150, 300
SSP : bc03 (G. Bruzual & S. Charlot 2003)	
Initial mass function (IMF)	Chabrier (G. Chabrier 2003)
Metallicity	0.02 (Z_{\odot}) , 0.008
Dust attenuation : dustatt_modified_CF00 (S. Charlot & S. M. Fall 2000)	
V-band attenuation in ISM (A_V^{ISM})	0.3, 0.5, 0.9, 1.1, 1.7, 2.0
μ	0.44
power law slope of attenuation in the ISM	-0.7, -1.3
power law slope of attenuation in the stellar birth clouds (BCs)	-0.7, -1.3
Dust emission : dl2014 (B. T. Draine et al. 2014)	
PAH mass fraction (q_{PAH} , in %)	2.5, 3.9, 4.58, 7.32
minimum radiation field (U_{min}) (Habing)	20, 25, 50
dust emission power law slope (α)	2, 3
fraction illuminated from U_{min} to U_{max} (γ)	0.02
AGN : fritz2006 (J. Fritz et al. 2006)	
ratio of the maximum to minimum radii of the dusty torus (r_{ratio})	60, 100, 150
equatorial optical depth at $9.7 \mu\text{m}$ (τ)	0.6, 10.0
radial dust distribution within the torus (β)	0.0
angular dust distribution within the torus (γ)	6
full opening angle of the dusty torus (Opening angle)	100
Angle between the equatorial axis and line of sight (Ψ)	0.001, 89.990
AGN fraction (f_{AGN})	0.0, 0.1, 0.15, 0.25, 0.5

4.2. Derived physical properties

The estimation of physical properties like stellar mass (M_{\star}), SFR (\dot{M}_{\star}), dust luminosity (L_{dust}) and dust mass (M_{dust}), of the *JWST*-detected simulated galaxies is done using CIGALE by setting the redshift to the value derived by EAZY. Also, we discuss the improvement that *JWST* NIRCcam photometry brings to the constraints on these physical parameters when complemented with the existing multiwavelength data from *HST*, *Spitzer* and *Herschel*. We make a comparative study of different combinations of photometry and analyse how *JWST* improves on those values. For each of the physical quantity, say P , we define the ratio of estimated (P^{CIGALE}) and true value (P^{input}) as

$$Q_{\log P} = \log \left(\frac{P^{\text{CIGALE}}}{P^{\text{input}}} \right) \quad (1)$$

We plot this ratio as a function of the true value. Moreover, we plot the histogram of this ratio. For each of the recovered physical properties, the median value along with the 1σ dispersion are reported in Table 3. Moreover, the median and RMS values of $Q_{\log P}$ for the different band combinations are explicitly reported in Table 4.

As far as the best-fit SED is concerned, we get a median reduced χ^2 value of $\sim 0.9 - 1.08$ for *JWST* and *JWST+HST* photometry, but when adding FIR photometry the value increases to ≈ 5 . The increase in reduced χ^2 when adding *Spitzer* and *Herschel* photometry to *JWST* and *HST* data in CIGALE betrays the fact that the UV-NIR and the far-IR/sub-mm bands preferentially see the emission from low- and high-obscuration regions, respectively. Also, while the *JWST* and the *HST* photometry are high-resolution and well-matched in aperture, the far-IR/sub-mm data have larger beam

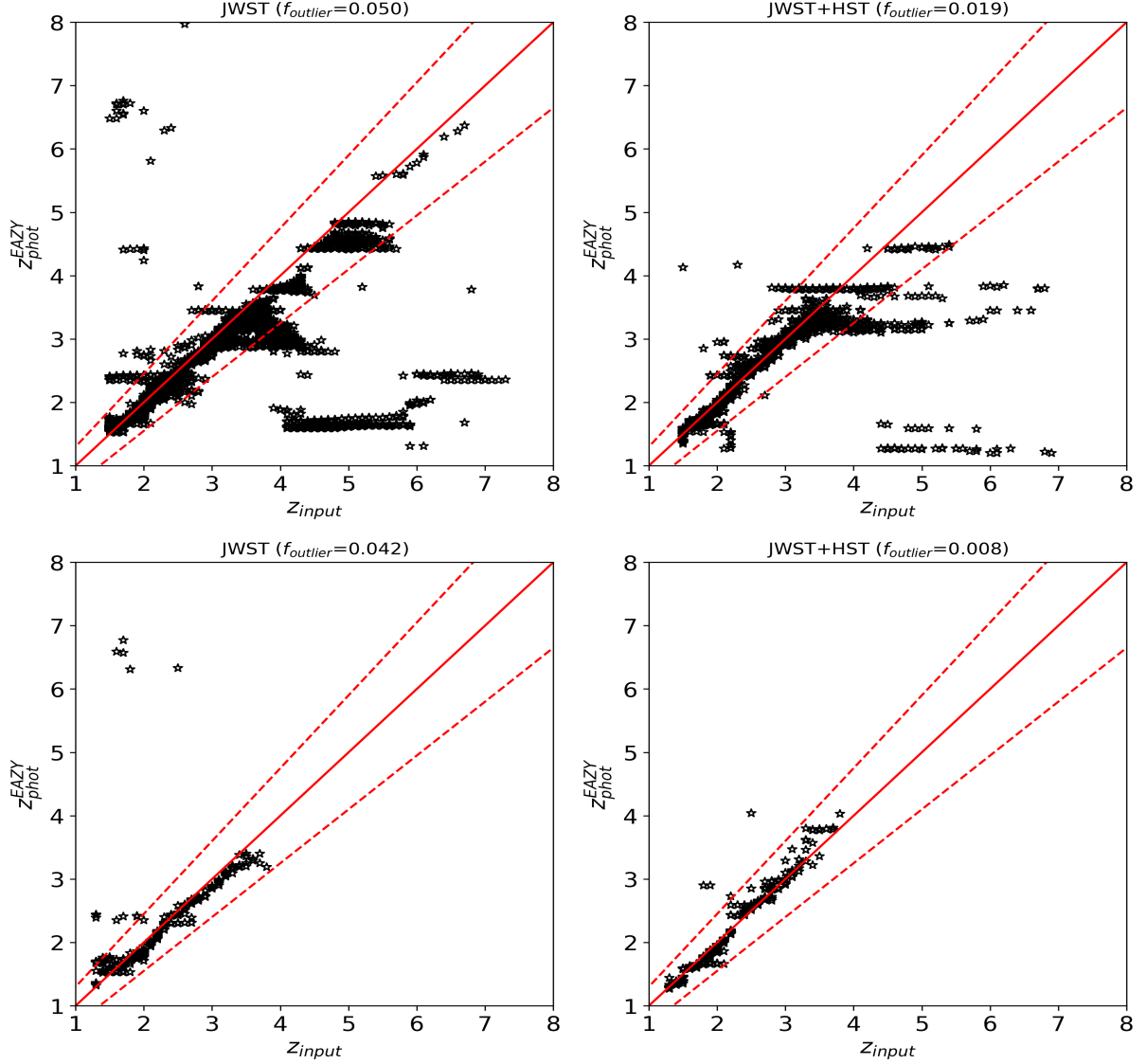


Figure 3. Derived photometric redshift using EAZY vs input redshift of the galaxies detected by *JWST* at $> 5\sigma$ in all 9 NIRCam bands, also detected by the *HST* at $\geq 5\sigma$ in the F435W and F160W bands. The solid red line denotes $z_{\text{input}} = z_{\text{phot}}^{\text{EAZY}}$ while the dashed red lines define the region where $|\Delta z| \leq 0.15(1 + z_{\text{input}})$. The top row refers to the parent sample while the bottom row is for DSFG sub-sample (detected at $\geq 5\sigma$ at $250\mu\text{m}$, i.e. having $S_{250\mu\text{m}} \geq 8.3\text{mJy}$). Most catastrophic outliers (black patches towards the bottom right of the top panel), i.e. sources having $z_{\text{input}} \gtrsim 4$ and low $z_{\text{phot}}^{\text{EAZY}}$, are AGN dominated. In other cases, catastrophic errors are due to the degeneracy between the Lyman- α break at 912 and the 4000 break.

sizes and potential blending issues. Our model does not allow us to deal with these issues because it yields a single, spatially-integrated SED for each source, i.e. the UV/NIR and FIR/sub-mm emission are co-located by construction.

CIGALE enforces energy balance between absorbed stellar light and dust re-emission. If the UV/optical fit suggests low dust attenuation, the model may struggle to match the observed IR fluxes, especially when the FIR SED shape or amplitude deviates from the assumed templates. Despite this higher reduced χ^2 , the uncertainties (dispersions) in key physical parameters like stellar mass

and SFR, which are the main focus of our study, remain low. This indicates that while the exact SED shape may not be perfectly reproduced across all bands, the overall physical interpretation is robust.

4.2.1. Stellar Mass

The scatter plots of the logarithm of the ratio between the estimated stellar mass ($M_{\star}^{\text{CIGALE}}$) and the input stellar mass (M_{\star}^{input}) as a function of M_{\star}^{input} for the parent and the DSFG sample are shown in Figures 4 and 5, respectively. The points are colour coded with their values of $|\Delta z|/(1 + z_{\text{input}})$. The histogram of

Table 3. Median values along with the median absolute deviation of the estimated physical quantities for the parent sample (where the simulated galaxies have virialised halo mass in the range $11.3 \leq \log(M_{\text{vir}}/M_{\odot}) \leq 13.3$) and the DSFG sub-sample (having flux density $\gtrsim 8.3$ mJy at $250 \mu\text{m}$), respectively.

	$\log(M_{\star}/M_{\odot})$	$\log(\dot{M}_{\star}/M_{\odot}\text{yr}^{-1})$	$\log(L_{\text{dust}}/L_{\odot})$	$\log(M_{\text{dust}}/M_{\odot})$
Parent Sample				
<i>JWST</i>	9.81 ± 0.16	-	-	-
<i>JWST+HST</i>	9.89 ± 0.23	-	-	-
Sub-sample				
<i>JWST</i>	10.8 ± 0.23	-	-	-
<i>JWST+HST</i>	10.86 ± 0.23	-	-	-
<i>Spitzer+Herschel</i>	-	2.21 ± 0.3	12.34 ± 0.26	8.5 ± 0.26
<i>HST+Spitzer+Herschel</i>	10.8 ± 0.3	2.5 ± 0.21	12.5 ± 0.23	8.5 ± 0.23
<i>JWST+Spitzer+Herschel</i>	10.83 ± 0.27	2.52 ± 0.22	12.48 ± 0.22	8.6 ± 0.22
<i>JWST+HST+Spitzer+Herschel</i>	10.83 ± 0.27	2.52 ± 0.23	12.5 ± 0.23	8.6 ± 0.23

Table 4. Mean (**median**) values of $Q_{\log P}$ for the parent sample (where the simulated galaxies have virialised halo mass in the range $11.3 \leq \log(M_{\text{vir}}/M_{\odot}) \leq 13.3$) and the DSFG sub-sample (having 5σ flux density $\gtrsim 8.3$ mJy at $250 \mu\text{m}$), respectively. The corresponding plots are shown in Figure 6, 8 and 11 respectively.

	$Q_{\log(M_{\star})}$	$Q_{\log(\dot{M}_{\star})}$	$Q_{\log(L_{\text{dust}})}$	$Q_{\log(M_{\text{dust}})}$
Parent Sample				
<i>JWST</i>	$-0.14(-\mathbf{0.132})$	-	-	-
<i>JWST+HST</i>	$-0.068(-\mathbf{0.083})$	-	-	-
Sub-sample				
<i>JWST</i>	$-0.004(-\mathbf{0.017})$	-	-	-
<i>JWST+HST</i>	$0.035(\mathbf{0.055})$	-	-	-
<i>Spitzer+Herschel</i>	-	$-0.196(-\mathbf{0.24})$	$0.075(\mathbf{0.085})$	$-0.012(-\mathbf{0.033})$
<i>HST+Spitzer+Herschel</i>	$0.01(-\mathbf{0.02})$	$0.037(\mathbf{0.056})$	$-0.006(-\mathbf{0.077})$	$0.124(\mathbf{0.12})$
<i>JWST+Spitzer+Herschel</i>	$-0.0169(-\mathbf{0.039})$	$0.044(\mathbf{0.032})$	$-0.049(-\mathbf{0.045})$	$0.15(\mathbf{0.13})$
<i>JWST+HST+Spitzer+Herschel</i>	$-0.04(-\mathbf{0.052})$	$0.053(\mathbf{0.066})$	$-0.066(-\mathbf{0.077})$	$0.13(\mathbf{0.13})$

$Q_{\log(M_{\star})}$, is also shown in the figures. When the stellar mass is derived from the *JWST* photometry alone, the 1σ dispersions in $Q_{\log(M_{\star})}$ are 0.2 and 0.14 for the parent catalogue and DSFG sample, respectively. CIGALE leans towards a slight but significant systematic underestimate of the stellar mass. Moreover, when using an exponentially declining SFH, stellar masses are often underestimated as was found by J. Pforr et al. (2012) while performing SED fitting on the semi-analytic model Galaxies In Cosmological Simulations (GalICS; S. Hatton et al. 2003).

We obtain the mean of $Q_{\log(M_{\star})}$ as -0.14 and -0.004 with *JWST* photometry for the parent and the DSFG sample, respectively. We observe that the 1σ dispersions reduce to 0.15 for the parent sample and 0.1 for the DSFG sample on removing the catastrophic photo- z outliers (AGN-dominated sources or power law like SEDs). Besides, the mean differences also reduce to -0.12 for the parent sample. As shown in Figure 6 (top panel) for the parent sample, including *HST* photometry along-

side *JWST* leads to a noticeable reduction in both the bias and scatter of stellar mass estimates, underscoring the value of extended NIR coverage in improving SED fitting accuracy. Combining the *JWST* with the *HST* photometry, the 1σ dispersion in $Q_{\log(M_{\star})}$ reduces to 0.14 for the parent sample, which after removal of outliers further decreases to 0.1. The mean difference becomes -0.068 and -0.063 respectively. This clearly shows that the dispersion in the stellar mass estimates is mainly due to the uncertainty in the photo- z . However, the overall estimation of stellar mass can also be affected by the difference in the slope of the dust attenuation law of the BCs used in CIGALE and the one used in our SED formalism (D. Mitra et al. 2024). Besides, the assumed SFH and its parameterisation also affects the estimation of stellar mass as pointed out by M. J. Michałowski et al. (2012) and S. Lower et al. (2020).

Moreover for the DSFG sample the 1σ dispersion reduces to 0.1 upon adding *HST* photometry to that of *JWST*. The mean offset is 0.035. Adding HST photome-

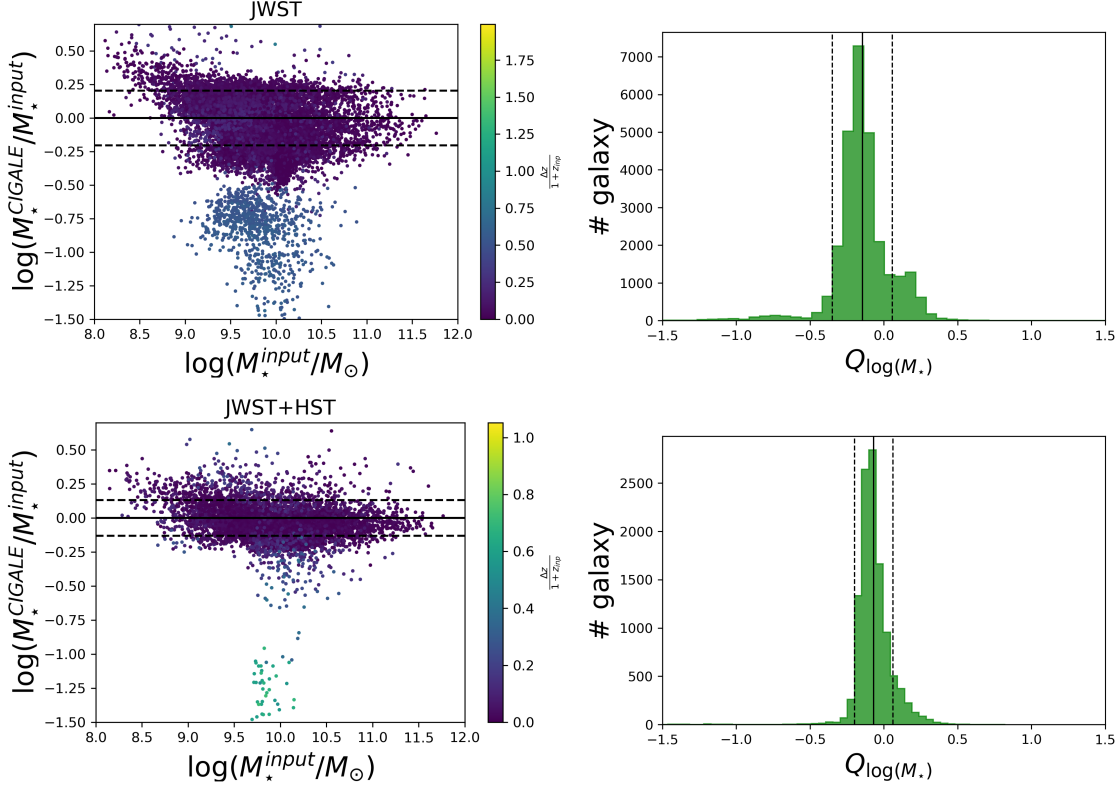


Figure 4. Scatter plot of the logarithm of the ratio between the estimated stellar mass ($M_{\star}^{\text{CIGALE}}$) and the input stellar mass (M_{\star}^{input}) as a function of M_{\star}^{input} for the parent sample of galaxies (i.e., $\log(M_{\text{vir}}/M_{\odot}) \geq 11.3$) from the *JWST* photometry (top row) and the *JWST+HST* photometry (bottom row). The points are colour-coded with their values of $|\Delta z|/(1+z_{\text{input}})$. The solid black line marks the locus of equality between the model values and the CIGALE estimated values. The boundaries of the 1σ dispersion around the mean are shown by the black dashed lines. The histograms of $Q_{\log(M_{\star})}$ are shown in the right-hand panels. The black solid line marks the mean value while the dashed lines denote the 1σ dispersion around the mean. Overall, CIGALE leans towards a slight but significant systematic underestimate of the stellar mass. In the top left panel, the small dark blue patch of sources having $\log(M_{\star}^{\text{CIGALE}}/M_{\star}^{\text{input}}) < -0.5$ and $9 \leq \log(M_{\star}^{\text{input}}/M_{\odot}) \leq 11$ is due to the sources which are AGN dominated and have catastrophic photo- z estimation errors ($|\Delta z|/(1+z_{\text{input}}) \gtrsim 0.5$) by EAZY. Similarly, such outliers are present in the bottom left panel seen as yellowish green patch ($|\Delta z|/(1+z_{\text{input}}) \gtrsim 0.6$) with $\log(M_{\star}^{\text{CIGALE}}/M_{\star}^{\text{input}}) < -1$ and $9.5 \leq \log(M_{\star}^{\text{input}}/M_{\odot}) \leq 10.5$.

try in the F435W and F160W bands to *JWST*/NIRCam data significantly improves the accuracy of stellar mass estimates by reducing key degeneracies in the SED fitting process. The F435W filter probes the rest-frame ultraviolet at redshifts $z \sim 1.5 - 3$, providing sensitivity to recent star formation and dust attenuation. This helps constrain the contribution of young stellar populations and mitigates the age-dust degeneracy that can otherwise bias mass estimates. The F160W filter, on the other hand, samples the rest-frame optical light and is crucial for capturing features like the Balmer and 4000Å breaks, which are strong indicators of older stellar populations that dominate the total stellar mass. Together, these two HST bands fill important gaps in wavelength coverage and complement the longer-wavelength NIRCam filters by anchoring both the blue and red ends of the SED. As a result, the stellar population properties

– particularly the mass-to-light ratio – are better constrained, leading to a measurable reduction in the 1σ dispersion of stellar mass estimates.

For the subsample, we also considered different combinations of photometry to estimate the stellar mass. The estimated stellar masses derived from the photometry from *HST*, *Spitzer* and *Herschel* have mean and median deviations from the true values of 0.01 and 0.23 in $Q_{\log(M_{\star})}$. An rms value and a mean value of 0.16 and -0.13 are obtained when using *JWST+Spitzer+Herschel* photometry. Estimating stellar mass from *HST+JWST+Spitzer+Herschel* photometry also gave a 1σ dispersion of 0.15 and a mean offset of -0.04 . Figure 6 (bottom panel) shows the recovery of stellar mass for the DSFG sub-sample using various photometric combinations. *JWST*/NIRCam photometry alone yields minimal bias and low scatter, highlight-

ing its strength in constraining stellar mass. Adding *HST* data does not significantly improve the estimates and introduces a slight positive bias. Legacy IR data without *JWST* result in larger scatter, while including *JWST* improves accuracy. As the evolved stellar populations dominate the stellar mass of galaxies and have most of their emission in the rest-frame optical/near-IR, the addition of far-IR photometry does not significantly improve the constraints on the stellar mass estimate. These findings underscore the remarkable capability of *JWST* in recovering the stellar mass of DSFGs.

4.2.2. SFR

The SFR of dust-enshrouded objects cannot be traced accurately using only the near-IR photometry (J. Pforr et al. 2012, 2013; Euclid Collaboration 2023; D. Mitra et al. 2024). In estimating the SFR, \dot{M}_\star , from *JWST* photometry, we obtain 1σ dispersions of ≈ 0.8 and 0.55 in $Q_{\log(\dot{M}_\star)}$ for the parent sample and sub-sample, respectively; the mean offsets are 0.14 and -0.05 , respectively. Adding the *HST* to *JWST* photometry, the 1σ dispersions reduce, but are still high with values of 0.36 and 0.47 for the two samples respectively. The mean differences are -0.044 and -0.019 . Therefore, complementing the *JWST* and/or the *HST* photometry with photometric data from FIR bands is crucial for estimating the SFR.

We now give estimates of SFR for different combinations of photometry for the DSFG sample only. For comparison, we also calculate the SFR from the FIR photometry alone. The mean and the 1σ dispersion of $Q_{\log(\dot{M}_\star)}$ are -0.196 and 0.22 for the *Spitzer* plus *Herschel* photometry. Adding the *HST* photometry to the above improves the estimation with the 1σ dispersion being 0.169 , and the mean reduces to 0.037 . Figure 7 shows the scatter plot of the logarithm of the ratio of estimated ($\dot{M}_\star^{\text{CIGALE}}$) to input SFR ($\dot{M}_\star^{\text{input}}$), colour coded with the values of $|\Delta z|/(1+z_{\text{input}})$. Also shown are the histogram of the ratio $Q_{\log(\dot{M}_\star)}$. Upon replacing *HST* with *JWST* in the above combination, we get a 1σ dispersion of 0.16 and a mean of 0.044 . However, when combining all the photometry from *JWST*+*HST*+*Spitzer*+*Herschel*, the dispersion increases to 0.18 and the mean becomes 0.053 .

The HST F435W and F160W filters sample the rest-frame UV and optical light at high redshift, which trace only the unobscured star formation. In DSFGs, this component is heavily suppressed and variable, leading to increased uncertainties and degeneracies in CIGALE’s energy balance when fitting both obscured and unobscured SFR components – thereby increasing the dispersion in total SFR estimates. Moreover, this increase

in the dispersion can also be due to the presence of some photo- z outliers in the sample.

A slight offset between the SFRs by CIGALE and the true values is expected, due to the different dust attenuation law slopes adopted by CIGALE and by E. da Cunha et al. (2008). However, our results show that the effect is minor. Figure 8 presents the accuracy of SFR recovery for the DSFG sub-sample using different combinations of photometric bands. The results show that using only *Spitzer* and *Herschel* data leads to higher dispersion and a slight underestimation of SFRs (we recall that in most cases, we have *Herschel* photometry only at $250\mu\text{m}$). The inclusion of *JWST* photometry significantly improves the estimates, reducing both bias and scatter. Adding *HST* data provides minimal additional benefit and may slightly worsen the results, likely due to the limited utility of rest-frame UV data in dust-obscured galaxies. Overall, these findings emphasize the crucial role of *JWST* in accurately constraining the SFRs of DSFGs.

Given that these galaxies are IR bright and dusty, the availability of robust far-IR/sub-mm data plays a vital role in the estimation of the SFR. Restricting the analysis of the SFR to the 33% sources from the DSFG sample detected by *Spitzer*+*Herschel* at $> 5\sigma$ in all *Spitzer*/MIPS and *Herschel* (PACS and SPIRE) bands gives a 1σ dispersion of 0.14 , 0.13 and 0.15 respectively in $Q_{\log(\dot{M}_\star)}$ for *Spitzer*+*Herschel*, *JWST*+*Spitzer*+*Herschel* and *JWST*+*HST*+*Spitzer*+*Herschel* photometry. Similarly, the 1σ dispersions in $Q_{\log(\dot{M}_{\star,10})}$ for these $> 5\sigma$ detected sources are 0.12 , 0.12 , and 0.15 respectively, for the same photometry combinations. Overall, we find that the SFR estimation was very challenging since it is very sensitive to the SFH (S. Lower et al. 2020). To verify this, we performed a test by keeping all the parameters of CIGALE unchanged and changing the assumed SFH from `sfhdelayed` to `sfhdelayedbq`⁴. Using `sfhdelayedbq` to estimate SFR we found that SFR is underestimated almost by an order of magnitude. When switching from `sfhdelayed` to `sfhdelayedbq` in CIGALE, the model allows for a recent burst or quenching event. For DSFGs, which typically have high, sustained SFRs, the burst/quench parameters can cause the fit to interpret their IR-luminous phase as a post-burst decline, leading to underestimated current SFRs. This misinterpretation happens because `sfhdelayedbq` may

⁴ The `sfhdelayed` module models a smooth, rising-and-declining star formation history, while `sfhdelayedbq` extends this by allowing for a recent burst or quenching event, making it more suitable for galaxies with abrupt SFR changes.

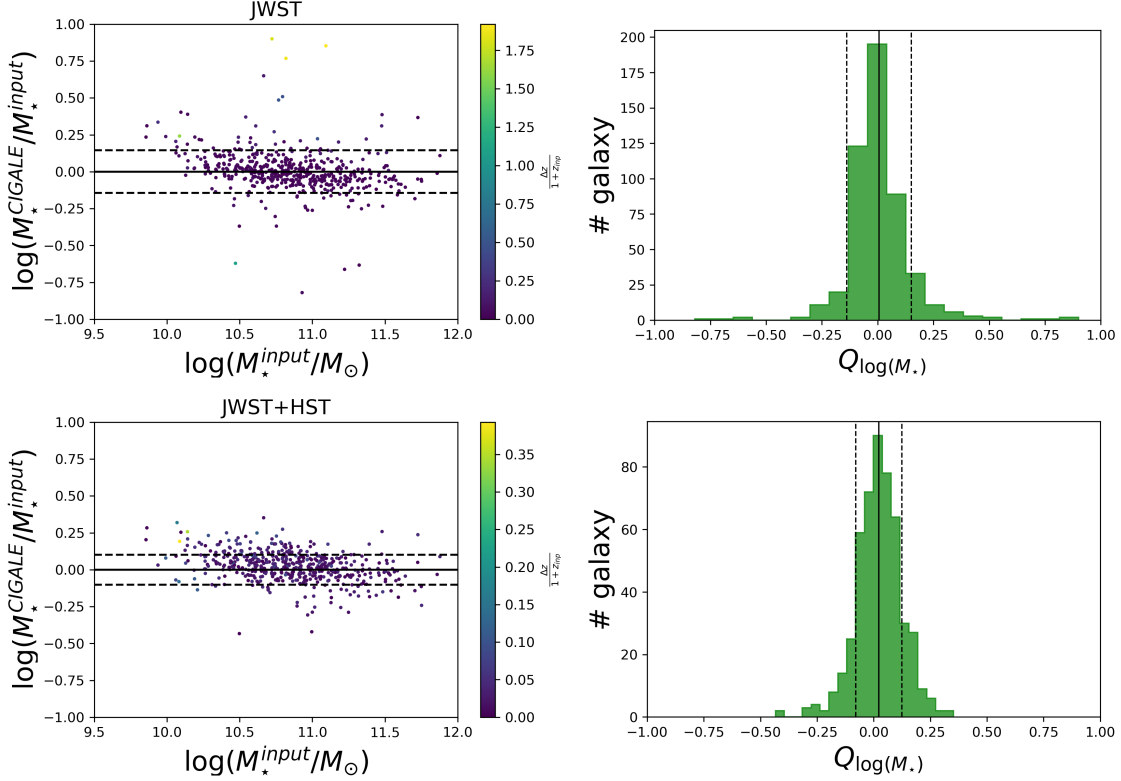


Figure 5. Scatter plot of the logarithm of the ratio of estimated stellar mass ($M_{\star}^{\text{CIGALE}}$) and the input stellar mass (M_{\star}^{input}) as a function of M_{\star}^{input} for the DSFG sample from the *JWST* photometry (top row) and the *JWST+HST* photometry (bottom row). The points are colour-coded with their values of $|\Delta z|/(1+z_{\text{input}})$. The histograms of $Q_{\log(M_{\star})}$, are shown in the right-hand panels. The meanings of the different line styles are the same as in Figure 4.

assign much of the star formation to an earlier burst, reducing the inferred ongoing SFR compared to the smoother `sfhdelayed` model. L. K. Hunt et al. (2019) argued that due to the sensitive nature of SFR to SFH, certain SED fitting algorithms may find it difficult to determine the most appropriate SFH due to degeneracies. Consequently, a range of different SFHs may yield comparably good SED fits.

4.2.3. Dust Luminosity and Dust Mass

The dust luminosity and the dust mass of our simulated DSFGs are computed using different combinations of photometric data: *Spitzer+Herschel*, *HST+Spitzer+Herschel*, *JWST+Spitzer+Herschel* and *JWST+HST+Spitzer+Herschel*. Figure 9 shows the distribution of $\log(L_{\text{dust}}^{\text{CIGALE}}/L_{\text{dust}}^{\text{input}})$ as a function of input L_{dust} along with the histogram of $Q_{\log(L_{\text{dust}})}$. With all the different combinations of photometry, we could recover the dust luminosity quite accurately with the 1σ dispersion in $Q_{\log(L_{\text{dust}})}$ being the least for *JWST+Spitzer+Herschel*, with a value of 0.12. The mean offset in this case is -0.049 . Upon adding the HST data to the above, the 1σ dispersion increases to 0.13 due to the photo- z outliers, and the mean offset

becomes -0.066 . Combining only *HST* data with FIR photometry, we get the dispersion value of 0.13 and a mean value of -0.06 . Only *Spitzer+Herschel* produces a mean value of 0.075 and a dispersion of 0.15. Overall, we observe that, upon adding UV/optical/NIR photometry, the dust extinction is better constrained, thus giving a more accurate estimate of L_{dust} as summarised in Figure 11 (top panel). From the values of the estimated median dust luminosity (see Table 3) we can categorise these galaxies as ultra-luminous infrared galaxies (ULIRGs).

The the distribution of $\log(M_{\text{dust}}^{\text{CIGALE}}/M_{\text{dust}}^{\text{input}})$ as a function of input M_{dust} along with the histogram of $Q_{\log(M_{\text{dust}})}$ is shown in Figure 10. The dust mass estimation has a larger dispersion compared to the dust luminosity (see Figure 11, bottom panel). The 1σ dispersions in $Q_{\log(M_{\text{dust}})}$ are 0.29, 0.27, 0.26 and 0.28 for the *Spitzer+Herschel*, *HST+Spitzer+Herschel*, *JWST+Spitzer+Herschel* and *JWST+HST+Spitzer+Herschel* photometry respectively, while the mean offsets are -0.012 , 0.124 , 0.150 , 0.130 . Overall, CIGALE gives an overestimation of dust mass which can be due to the difference in the

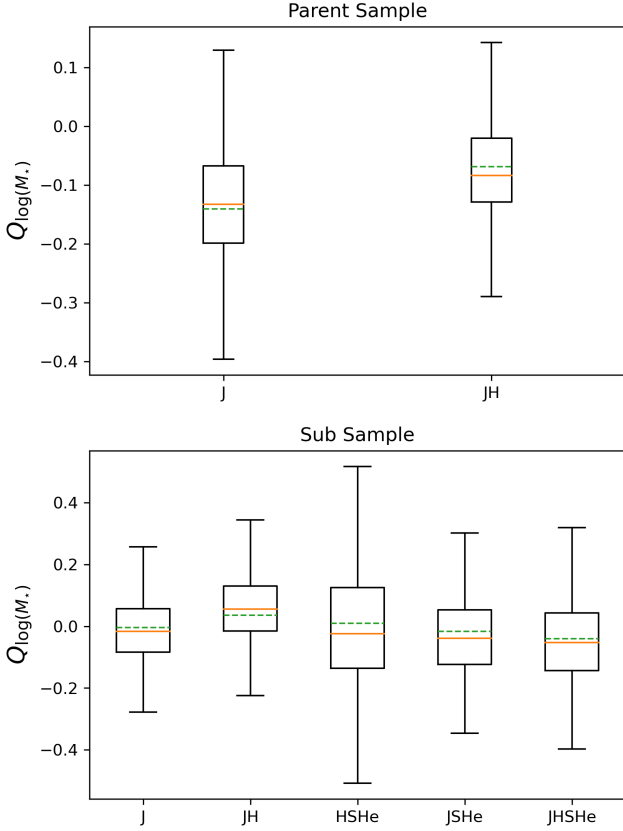


Figure 6. Boxplot showing the distribution of the $Q_{\log(M_*)}$, for the parent sample (top panel) using *JWST* and *JWST+HST* photometry and the DSFG sample (bottom panel) using *JWST*, *JWST+HST*, *JWST+Spitzer+Herschel* and *JWST+HST+Spitzer+Herschel* photometry. The solid orange line denotes the median, while the dashed green line represents the mean. The interquartile range and whiskers indicate the spread and outliers of the distribution. Here the abbreviations in the labels are: J - *JWST*, JH - *JWST+HST*, JSHe - *JWST+Spitzer+Herschel* and JHSHe - *JWST+HST+Spitzer+Herschel*.

value of the reference emissivity of dust grains per unit mass, κ_0 , adopted by the two SED fitting codes (C.-L. Liao et al. 2024). Moreover, L. K. Hunt et al. (2019) while comparing various SED fitting models by fitting far-UV to sub-mm photometry data of 61 KINGFISH galaxies found that CIGALE overestimates M_{dust} as compared to MAGPHYS (based on E. da Cunha et al. (2008) SED formalism) due to the absence of agreement regarding dust opacity.

Also, from Figure 10 it is observed that there is a negative correlation between $\log(M_{\text{dust}}^{\text{CIGALE}}/M_{\text{dust}}^{\text{input}})$ and $\log(M_{\text{dust}}^{\text{input}})$. This negative correlation is likely due to the assumption of fixed dust absorption coefficient (κ) and emissivity index (β) by CIGALE. S. Bianchi et al. (2022) pointed out the need for more realistic dust

emission models that consider the temperature distribution and varying dust opacity across different environments. We note that the discrepancy between $M_{\text{dust}}^{\text{CIGALE}}$ and $M_{\text{dust}}^{\text{input}}$ is more prominent for $\log(M_{\text{dust}}^{\text{input}}) \lesssim 8.5$, where CIGALE substantially overestimates M_{dust} . For $\log(M_{\text{dust}}^{\text{input}}) \gtrsim 9$ the negative correlation is not significant. To further explore this effect, we performed a test comparing the logarithmic ratios of dust mass and dust temperature estimated by CIGALE to those from our model. Our model uses a three-component dust temperature to calculate the dust mass whereas CIGALE models the dust emission using a range of interstellar radiation field intensities (U). To define a single dust temperature from our model, we calculate the mass-weighted dust temperature as

$$T_{\text{dust}}^{\text{inp}} = \frac{(M_{\text{dust},W}^{\text{BC}} T_{w,\text{BC}} + M_{\text{dust},W}^{\text{ISM}} T_{w,\text{ISM}} + M_{\text{dust},c}^{\text{ISM}} T_{c,\text{ISM}})}{(M_{\text{dust},W}^{\text{BC}} + M_{\text{dust},W}^{\text{ISM}} + M_{\text{dust},c}^{\text{ISM}})} \quad (2)$$

For more details about the model calculation of dust mass and the meanings of the above symbols, we refer the readers to D. Mitra et al. (2024). To calculate the dust temperature estimated by CIGALE, we use the best fit mean intensity U_{mean} in the relation from B. T. Draine et al. (2014)

$$T_{\text{dust}}^{\text{CIGALE}} = 18 U_{\text{mean}}^{\frac{1}{6}} \quad (3)$$

We then compute $Q_{\log(T_{\text{dust}})} = \log(T_{\text{dust}}^{\text{CIGALE}}/T_{\text{dust}}^{\text{inp}})$ and compute its correlation with $Q_{\log(M_{\text{dust}})}$. We observe a clear negative correlation between $Q_{\log(M_{\text{dust}})}$ and $Q_{\log(T_{\text{dust}})}$ as shown in Figure 12, consistent with the known degeneracy in SED fitting. This anti-correlation indicates that when CIGALE infers a higher dust temperature relative to our model, it tends to infer a lower dust mass, and vice versa. This is because, for a given FIR luminosity, higher temperatures require less dust to produce the same emission and models must compensate accordingly. This trend highlights that differences in dust temperature assumptions can significantly impact the inferred dust masses, even when the overall FIR luminosities are matched.

The estimated dust mass from the different photometry combinations of our simulated sources has a median value of $\log(M_{\text{dust}}/M_{\odot}) \gtrsim 8.5$. Similar dust mass estimates were obtained by E. da Cunha et al. (2015) while studying with *ALMA* a sample of 122 870 μm -detected sources in the Extended Chandra Deep Field South. A. M. Swinbank et al. (2014) also reported dust mass estimates consistent with ours while studying the far-IR properties of a sample of 99 SMGs in the Extended

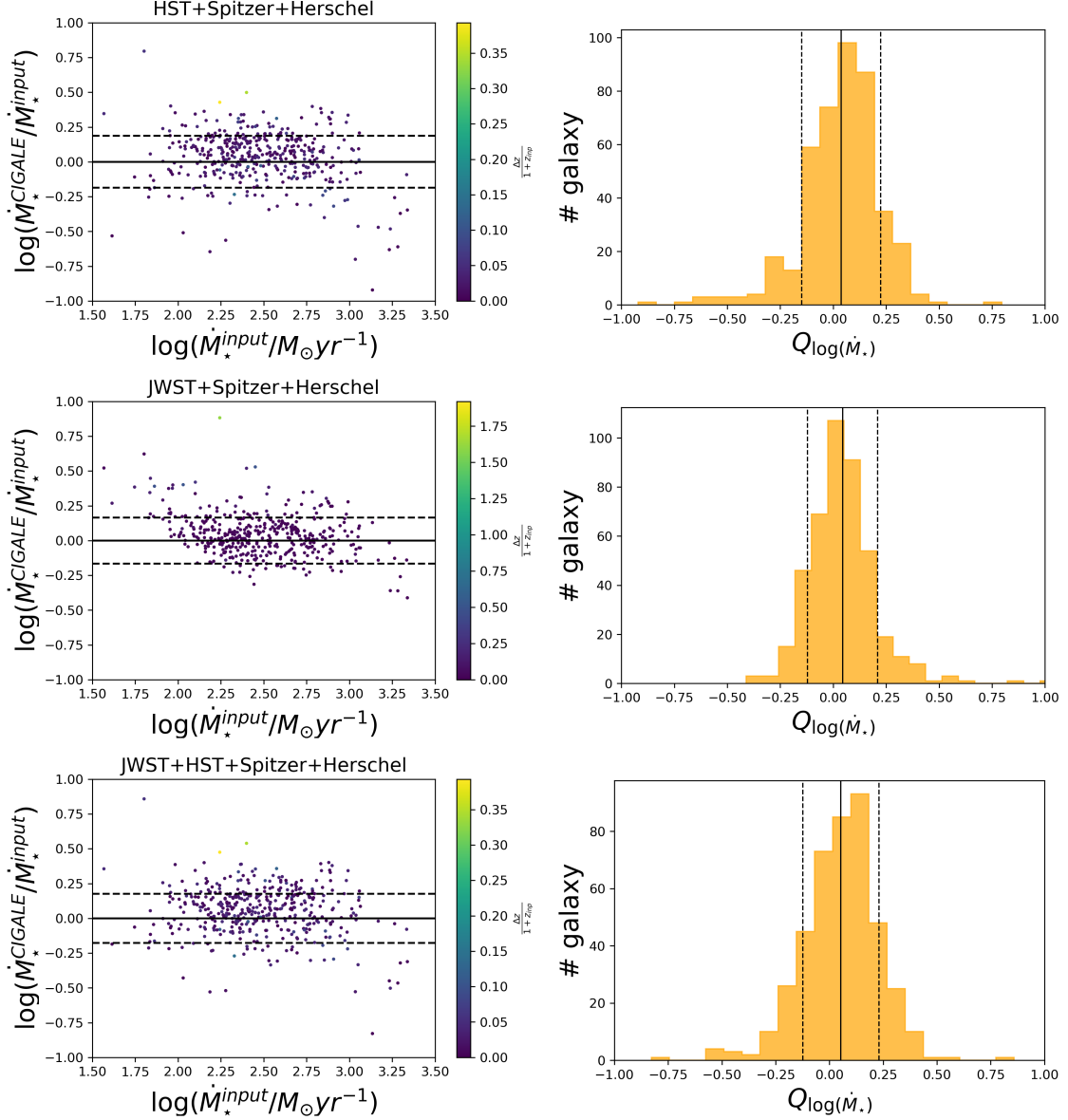


Figure 7. Scatter plot of the logarithm of the ratio of estimated ($\dot{M}_{\star}^{\text{CIGALE}}$) to input ($\dot{M}_{\star}^{\text{input}}$) SFR obtained for the DSFG sample from *HST*+*Spitzer*+*Herschel*, *JWST*+*Spitzer*+*Herschel* and *JWST*+*HST*+*Spitzer*+*Herschel* photometry. The points are colour-coded with their values of $|\Delta z|/(1+z_{\text{input}})$. The histogram of $Q_{\log(\dot{M}_{\star})}$, is also shown in the figures. The meaning of the different line styles is the same as in Figure 4.

Chandra Deep Field South at 870 μm with *ALMA*. In general, these galaxies have a higher dust content than the low- z ($z < 1$) galaxies, as was shown by K. Rowlands et al. (2014).

4.3. Comparison with physical properties of DSFG sources in the ASTRODEEP-*JWST* catalog

To enable a realistic comparison between observed and simulated DSFGs, we constructed a catalog of DSFG counterparts based on the ASTRODEEP-*JWST* photometric catalog by applying near-infrared colour selection criteria optimized for identifying dusty galaxies, follow-

ing the method described by A. J. Barger & L. L. Cowie (2023). These criteria are tailored to select DSFGs using only NIRCcam bands, providing a practical strategy for identifying heavily dust-obscured galaxies in *JWST* surveys where far-IR data may be limited. In parallel, we applied the same selection criteria to our simulated DSFG subsample to generate a corresponding mock catalog that mimics the observational selection. For both the observed and simulated samples, we performed SED fitting using CIGALE, incorporating the same model assumptions and wavelength coverage, in order to derive physical parameters such as stellar mass and SFR. This

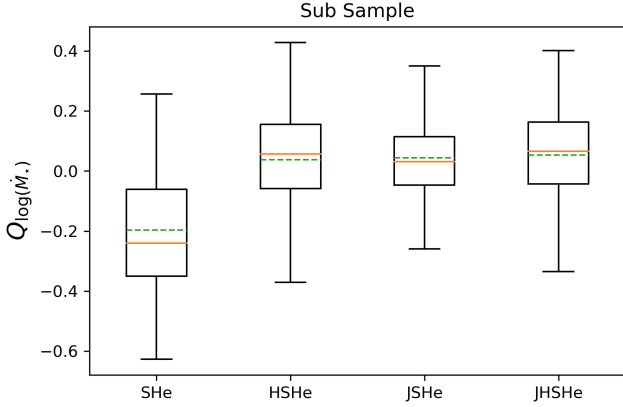


Figure 8. Boxplot showing the distribution of the $Q_{\log(M_*)}$ for the DSFG sample using *HST*+*Spitzer*+*Herschel* (SHHe), *JWST*+*Spitzer*+*Herschel* (JSHe) and *JWST*+*HST*+*Spitzer*+*Herschel* (JHSHe) photometry. The solid orange line denotes the median and the dashed green line indicates the mean. The interquartile range and whiskers indicate the spread and outliers of the distribution.

procedure ensures a fair comparison between the simulated and observed populations under identical selection and fitting conditions, allowing us to assess the reliability of our modeling framework in reproducing the physical properties of *JWST*-selected DSFGs.

The ASTRODEEP-*JWST* catalog provides photometric redshift estimates using EAZY and ZPHOT (A. Fontana et al. 2000) based on *JWST* NIRCам and *HST* photometry for sources in 6 extragalactic deep fields including GOODS-S, aimed at studying the high redshift Universe. The catalog comprises all sources detected at 5σ in the NIRCам F444W band. The GOODS-S catalog consists of 73 638 sources in the redshift range $0 \leq z \leq 20$. As our simulations are limited to the range $1 \leq z \leq 8$ (for more details see D. Mitra et al. (2024)), we considered only the 55 028 ASTRODEEP sources within this range.

The NIRCам A. J. Barger & L. L. Cowie (2023) photometric criteria for selecting DSFG is defined as follows:

$$S_{F444W}/S_{F150W} > 3.5, S_{F444W} > 1 \mu\text{Jy} \quad (4)$$

By applying the above selection criteria to both the ASTRODEEP-*JWST* catalog and the simulated sample we create a sample of NIRCам DSFGs having 866 and 516 galaxies respectively. This colour selection along with the distribution of sources both in the ASTRODEEP-*JWST* catalog and the simulated sample is shown in Figure 13.

For the estimation of physical properties of the ASTRODEEP NIRCам DSFGs sources we used the same modules of CIGALE specified in subsect. 3.3. For these ASTRODEEP sources, the estimated stellar mass and

SFR have a median value of $\log(M_*/M_\odot) = 10.12 \pm 0.3$ and $\log(\dot{M}_*/M_\odot\text{yr}^{-1}) = 2.4 \pm 0.4$ respectively. For the simulated NIRCам DSFGs, the estimated stellar mass and SFR have a median value of $\log(M_*/M_\odot) = 10.3 \pm 0.3$ and $\log(\dot{M}_*/M_\odot\text{yr}^{-1}) = 2.0 \pm 0.3$ respectively.

Figure 14 shows the histograms of stellar masses and SFRs of both the ASTRODEEP and the simulated DSFGs as a function of redshift. The distributions of stellar mass and SFR for the ASTRODEEP and the simulated sources are in good agreement. This overall agreement between the simulated DSFG sample and the NIRCам-selected DSFGs from the ASTRODEEP catalog highlights the consistency of the simulation framework with observational data. Furthermore, this comparison underscores the efficacy of *JWST* in detecting DSFGs with stellar masses as low as $\sim 10^{10} M_\odot$.

5. SUMMARY AND CONCLUSIONS

We have investigated the ability of the *JWST* to study the properties of $z > 1.5$ progenitors of present-day massive spheroidal galaxies, using the JADES survey strategy in the GOODS-S field. We also analysed the effect of complementing *JWST* data with the data from previous surveys with *HST*, *Spitzer* and *Herschel*. Our analysis is based on the physical model by Z.-Y. Cai et al. (2013) for the evolution of proto-spheroidal galaxies, as upgraded by D. Mitra et al. (2024). We have found that our model is consistent with the recent observations of MIR LFs of these high- z galaxies.

Using the model, we simulated a sample of proto-spheroidal galaxies, which we called the parent sample, with $\log(M_{\text{vir}}/M_\odot) \gtrsim 11.3$ and $z \geq 1.5$, over a survey area of 87.5 sq. arcmin., similar to the area covered by JADES-Medium in the GOODS-S field. According to the model, at the 5σ detection limit in the 9 NIRCам filters chosen for JADES, *JWST* detects 27748 galaxies of which about 41% are also detected by *HST* above 5σ in the F435W and F160W bands. In this sample, only about $\sim 2\%$ of the *JWST* sources are detected at $> 5\sigma$ by *Spitzer* and *Herschel*. So, to include the photometry from the above IR instruments, we focused on the sub-sample of galaxies with $\log(M_{\text{vir}}/M_\odot) \gtrsim 12$, as *Herschel* did not detect DSFGs below that threshold anyway. From this sub-sample, we constructed a DSFG sample by selecting galaxies that are detected at $\geq 5\sigma$ at $250 \mu\text{m}$ with *Herschel*. This yielded 507 simulated dusty galaxies. Among these, 503 galaxies ($\sim 99\%$) are also detected at 5σ in all nine NIRCам bands, and approximately 98.8% are detected by *HST*. Furthermore, 434 galaxies ($\sim 86\%$) in this DSFG sample are simultaneously detected at $> 5\sigma$ in both *Spitzer*/MIPS bands.

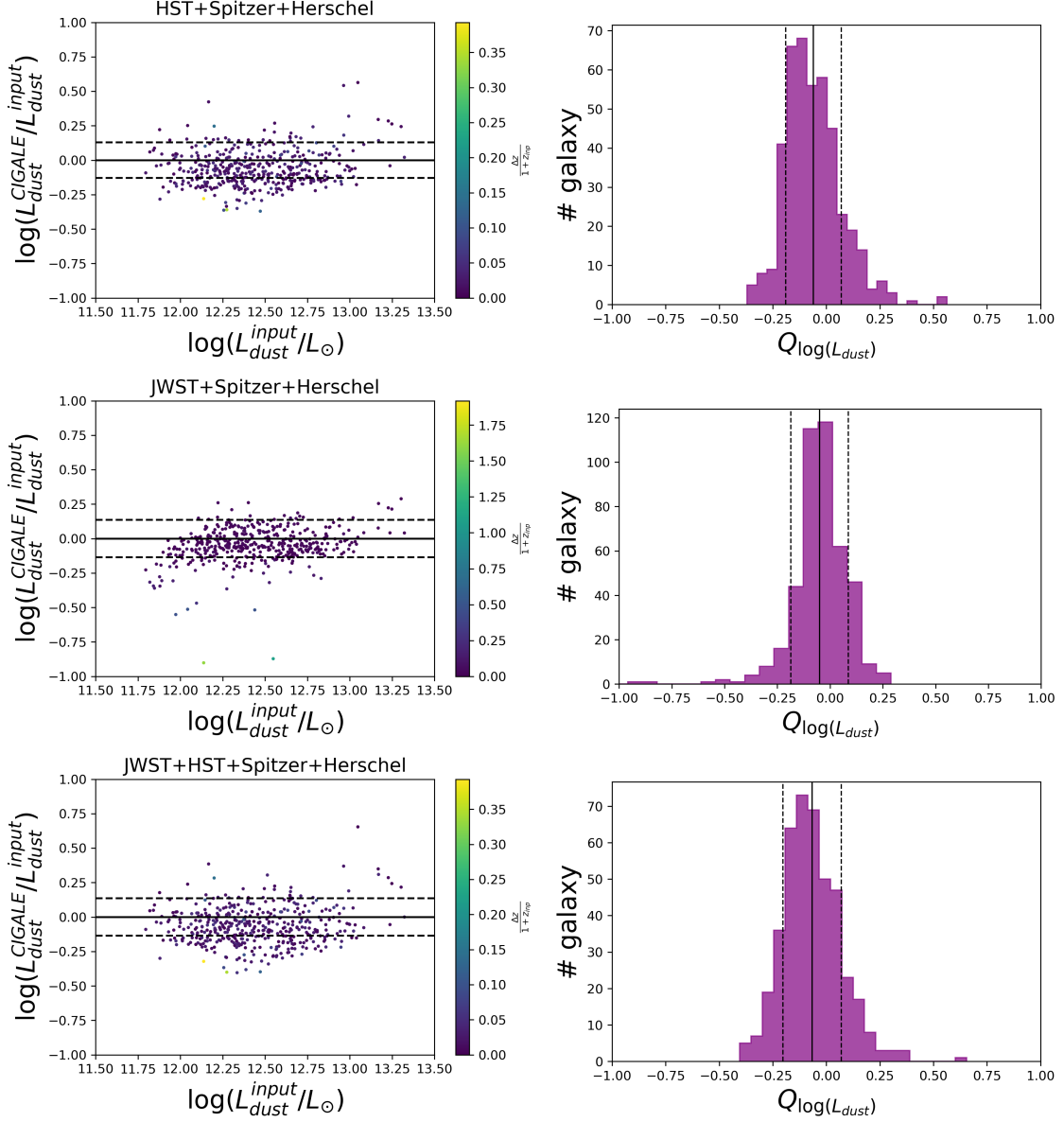


Figure 9. Same as Figure 7, but for the dust luminosity (L_{dust}).

The first thing we estimated for our simulated DSFGs was the photometric redshift. For that, we used EAZY on the *JWST* photometry alone as well as on the *JWST*+*HST* photometry. Then we estimated the physical properties using the code CIGALE and different combinations of photometric data: *JWST*, *JWST*+*HST*, *Spitzer*+*Herschel*, *HST*+*Spitzer*+*Herschel*, *JWST*+*Spitzer*+*Herschel* and *JWST*+*HST*+*Spitzer*+*Herschel*. Our findings are as follows

1. We found that for 90% of the sources detected by *JWST* at 5σ , EAZY gave a good estimate of the photometric redshift with the accuracy in $(1+z)$ being better than 15%. Catastrophic out-

liers in the $4 \leq z \leq 6$ range were mostly due to the degeneracy between the Lyman break and the 4000 break. Upon addition of the *HST* photometry to the *JWST* data, most catastrophic outliers were removed; in fact, by adding filters blueward of $0.7 \mu\text{m}$, the Lyman break could be properly sampled. We got a more accurate estimate of redshift, with $< 15\%$ discrepancy in $(1+z)$ for $\gtrsim 98\%$ sources detected by both *JWST* and *HST*. Catastrophic error estimates are then limited to the 1–2% AGN-dominated sources. For the DSFG sample, *JWST* provided estimates of the photometric redshift with the accuracy in $(1+z)$ being

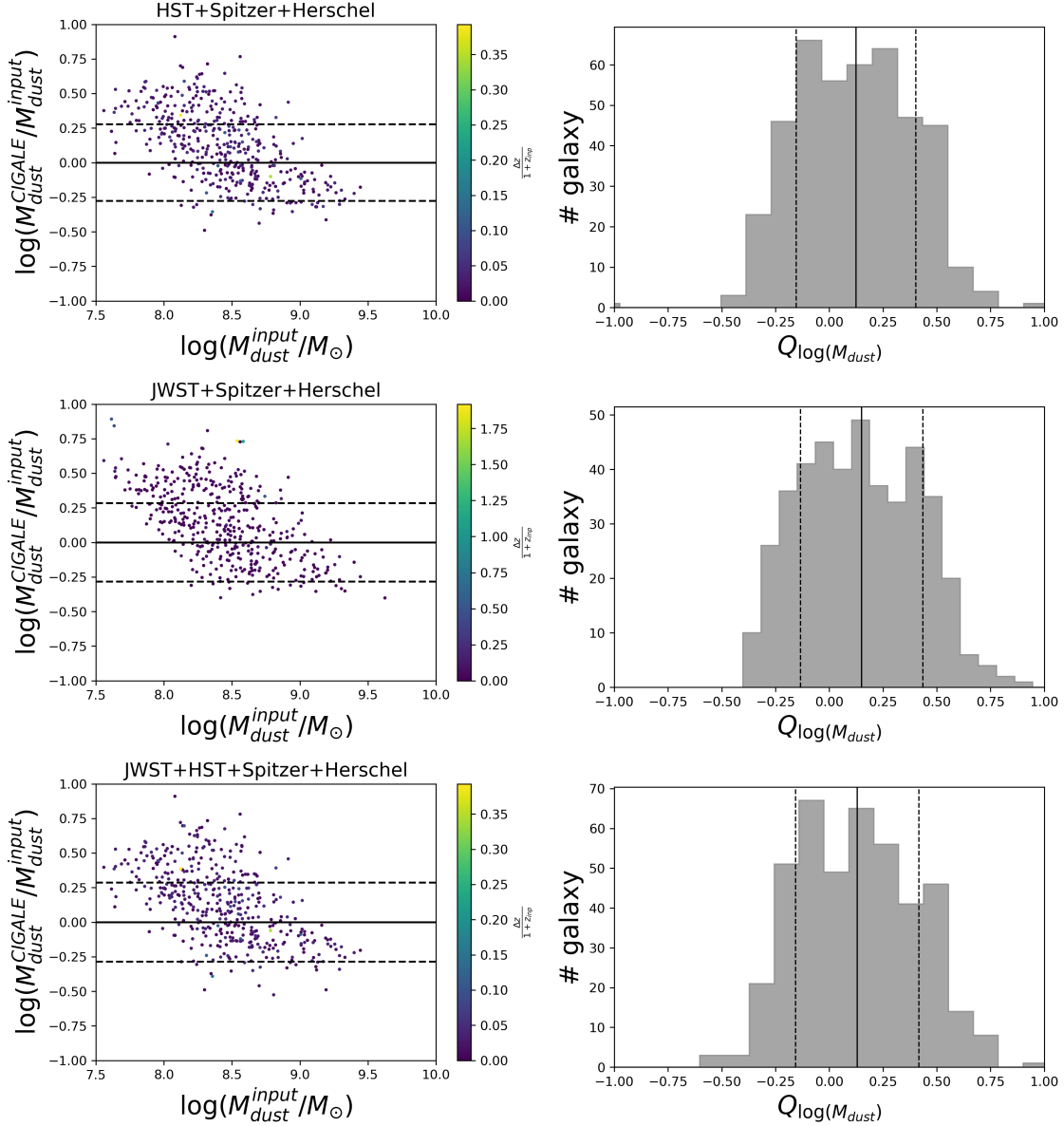


Figure 10. Same as Figure 7, but for the dust mass (M_{dust}).

better than 15% for $\gtrsim 95\%$ sources, which further increased to $\sim 99\%$ upon adding *HST* photometry.

- Using the *JWST* photometry alone, $\log(M_{\star}^{\text{CIGALE}}/M_{\star}^{\text{input}})$ has a 1σ dispersion of ≈ 0.2 for the parent sample and 0.14 for the sub-sample respectively. On removing the photo- z outliers, the 1σ dispersion reduces to ≈ 0.15 and 0.1 respectively. This clearly shows the direct effect of wrong photo- z estimation on the estimation of stellar mass. As expected, adding the sub-mm photometry from *Spitzer* and *Herschel* produced little improvement on the stellar mass estimate. Adding the *HST* photometry to that

of *JWST*, the stellar mass could be recovered relatively well with a 1σ dispersion as low as 0.14 for the parent sample and 0.1 for the sub-sample; also the mean offset between true and estimated stellar masses decreases. This shows that, as expected, the stellar mass is more sensitive to rest-frame UV/optical/near-IR wavelengths than to the far-IR/sub-mm part of the SED.

- The SFR cannot be accurately derived from the *JWST* photometry alone: the rms dispersion of $Q_{\log(M_{\star})} = \log(M_{\star}^{\text{CIGALE}}/M_{\star}^{\text{input}})$, is 0.55. The addition of the *HST* photometry leads to a modest improvement, but the dispersion remains high. Only FIR/sub-mm data from *Spitzer*/MIPS and

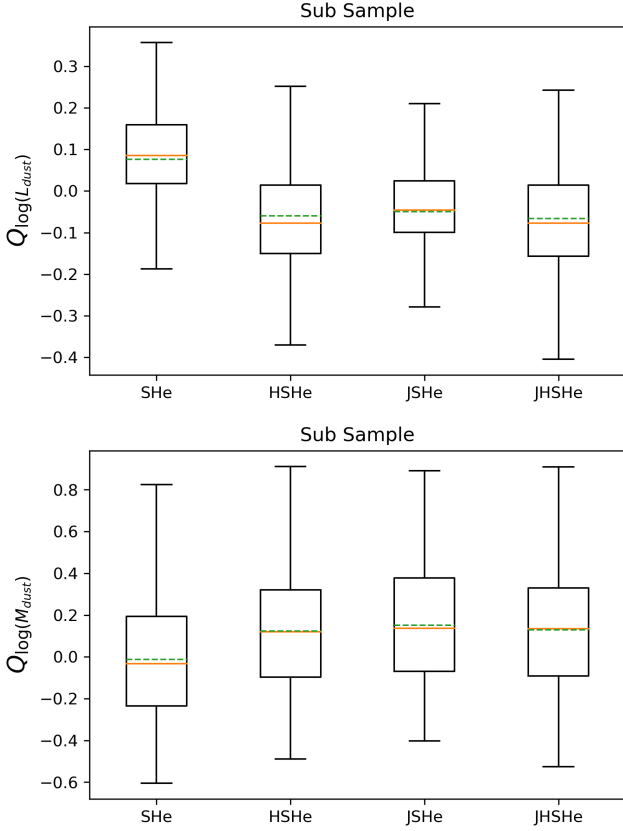


Figure 11. Same as Figure 8, but for the dust luminosity (L_{dust} , top panel) and dust mass (M_{dust} , bottom panel).

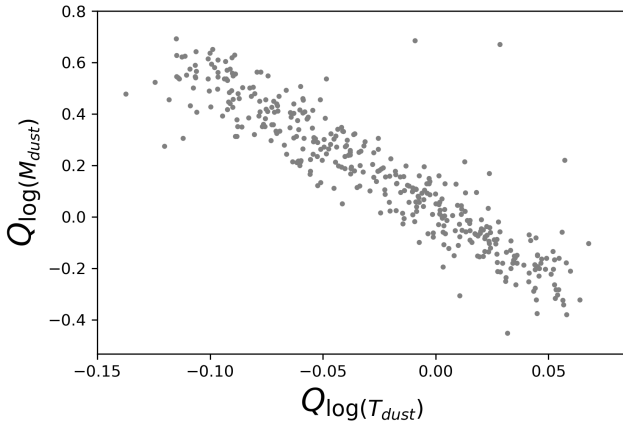


Figure 12. Scatter plot showing the correlation between $Q_{\log(M_{\text{dust}})}$ and $Q_{\log(T_{\text{dust}})}$. A clear negative trend is observed, highlighting the degeneracy between dust mass and dust temperature in SED fitting. This indicates that when CIGALE estimates a higher dust temperature relative to the input model, it compensates by assigning a lower dust mass, and vice versa.

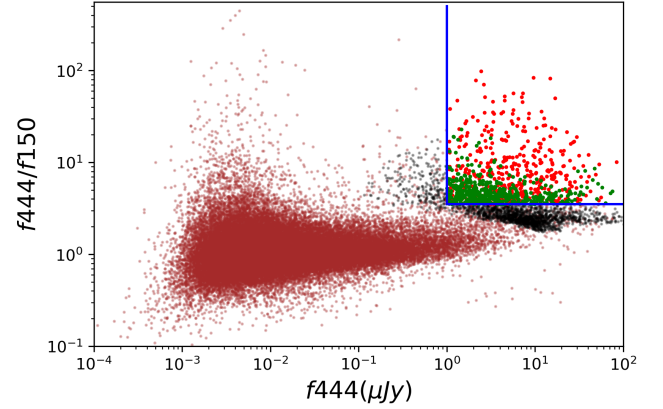


Figure 13. Colorflux diagram for NIRCcam DSFG selection showing the ratio f_{444}/f_{150} vs f_{444} (in μJy) for galaxies in the simulated (black points) and ASTRODEEP (brown points) sample. Red points correspond to NIRCcam DSFG candidates from ASTRODEEP sample, while green points represent NIRCcam DSFG candidates from the simulated sample. The A. J. Barger & L. L. Cowie (2023) selection criteria is shown in blue lines.

Herschel (PACS and SPIRE) allowed us to decrease the dispersion in $Q_{\log(\dot{M}_*)}$ to 0.16–0.18. As expected, the availability of robust FIR/sub-mm photometry is crucial for constraining the SFR accurately. Unfortunately, these data are available only for a tiny fraction of the sample. On the other hand, we found that the FIR/submm photometry alone yields a dispersion of 0.22, demonstrating that the addition of *JWST* data significantly improves the accuracy. On the whole, the sampled sources have a median SFR $\log(\dot{M}_*/M_{\odot}\text{yr}^{-1}) \sim 2.5$, clearly showing that these galaxies are going through intense star formation activity.

4. Dust luminosity and dust mass could only be estimated for sources having *Spitzer* and *Herschel* photometry. The estimated dust luminosity has a median value of $\log(L_{\text{dust}}/L_{\odot}) \sim 12.5$, while the median value of the estimated dust mass is $\log(M_{\text{dust}}/M_{\odot}) \sim 8.5$, showing that these DSFGs at $z \gtrsim 1.5$ are highly luminous and are more heavily dust-enshrouded than $z \sim 1$ galaxies. Again, the addition of *JWST* data improves the accuracy. Estimates of dust masses are affected by the substantial uncertainty on the value of the reference emissivity of dust grains per unit mass. It is also affected by dust temperature assumptions.
5. Our estimates of stellar mass and SFR for the ASTRODEEP-*JWST* sources demonstrate the capability of *JWST* to detect high- z galaxies with stellar mass almost an order of magnitude lower

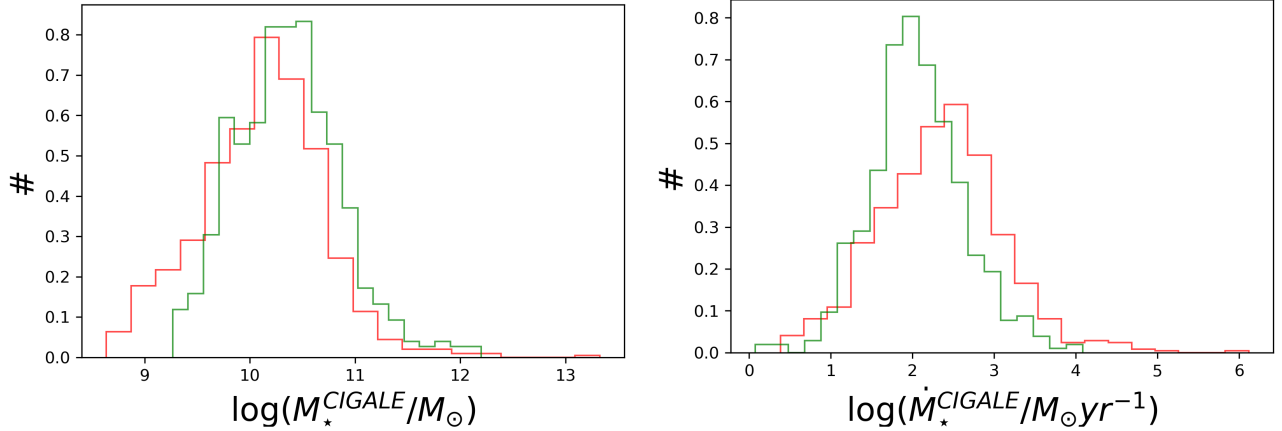


Figure 14. Normalized distribution of stellar masses (left) and SFR (right) derived from CIGALE for the simulated (green) and the ASTRODEEP (red) NIRCcam-selected DSFGs.

than possible in the pre-*JWST* era. The comparison of the estimated physical properties of the ASTRODEEP sources and our simulated sources shows a good level of consistency between the two.

Therefore, in this work, we have shown that, in the GOODS-S field, *JWST* alone can well constrain the stellar mass of massive DSFGs. The estimates of the physical properties of DSFGs can be improved by exploiting the rich *HST*, *Spitzer* and *Herschel* data available from previous surveys like CANDELS. To recover the IR properties of DSFGs, the *JWST* and *HST* data should be complemented with those from *Spitzer* and *Herschel*; however, deeper far-IR/sub-mm data are badly needed. Overall, it can be concluded that *JWST* can enrich the study of DSFGs by producing tighter constraints on the physical properties and revealing fainter, lower-mass dusty galaxies previously inaccessible to *Herschel* or *Spitzer*.

This work clearly demonstrates the transformative role of *JWST* in advancing our understanding of dusty galaxy populations at high redshift. Nonetheless, it also highlights the limitations imposed by the lack of sufficiently deep far-infrared and submillimetre observations. Future facilities such as the proposed *PRIMA* or next-generation ground-based sub-mm observatories will be crucial for probing the peak of dust emission and disentangling the star formation and AGN components more robustly. Continued development of sensi-

tive, high-resolution IR probes will further complement the capabilities of *JWST*, enabling a more complete census of the dust-obscured universe and enhancing our ability to trace galaxy evolution across cosmic time. A critical problem for space-borne far-IR/sub-mm probes is angular resolution. A promising perspective is offered by far-IR interferometry, that can achieve sub-arcsec resolution (D. Leisawitz et al. 2008; M. Bonato et al. 2024).

ACKNOWLEDGMENTS

DM acknowledges the postgraduate studentship provided by the UK Science and Technology Facilities Council (STFC). In this work, we have used the following Python packages: *Astropy*⁵ (Astropy Collaboration 2013, 2018, 2022), *Scipy*⁶ (E. Jones et al. 2001), *Numpy*⁷ (S. van der Walt et al. 2011; C. R. Harris et al. 2020), *Joblib*⁸, *COLOSSUS*⁹ (B. Diemer 2018), *Seaborn*¹⁰ (M. Waskom 2021) and *Matplotlib*¹¹ (J. D. Hunter 2007). The authors would like to thank the anonymous referee for the thorough review and constructive feedback, which helped to refine the manuscript.

AUTHOR CONTRIBUTIONS

DM was responsible for the analysis and modelling as well as the preparation and presentation of this manuscript. MN and GDZ contributed to the interpretation and the overall development of the manuscript.

⁵ <https://www.astropy.org/>

⁶ <https://scipy.org/index.html>

⁷ <https://numpy.org/>

⁸ <https://joblib.readthedocs.io/en/stable/>

⁹ <https://pypi.org/project/colossus/>

¹⁰ <https://seaborn.pydata.org/index.html>

¹¹ <https://matplotlib.org/>

REFERENCES

- Alberts, S., Rujopakarn, W., Rieke, G. H., Jagannathan, P., & Nyland, K. 2020, *The Astrophysical Journal*, 901, 168
- Amvrosiadis, A., Wardlow, J. L., Birkin, J. E., et al. 2025, *MNRAS*, 536, 3757
- Astropy Collaboration. 2013, *Astronomy and Astrophysics*, 558, A33
- Astropy Collaboration. 2018, *The Astronomical Journal*, 156, 123
- Astropy Collaboration. 2022, *The Astrophysical Journal*, 935, 167
- Barger, A. J., & Cowie, L. L. 2023, *The Astrophysical Journal*, 956, 95
- Barger, A. J., Cowie, L. L., Sanders, D. B., et al. 1998, *Nature*, 394, 248
- Barro, G., Prez-Gonzalez, P. G., Cava, A., et al. 2019, *The Astrophysical Journal Supplement Series*, 243, 22
- Beckwith, S. V. W., Stiavelli, M., Koekemoer, A. M., et al. 2006, *The Astronomical Journal*, 132, 17291755
- Bernardi, M., Shankar, F., Hyde, J. B., et al. 2010, *MNRAS*, 404, 2087
- Bianchi, S., Casasola, V., Corbelli, E., et al. 2022, *Astronomy and Astrophysics*, 664, A187
- Birkin, J. E., Puglisi, A., Swinbank, A. M., et al. 2024, *MNRAS*
- Bonato, M., Leisawitz, D., De Zotti, G., et al. 2024, *ApJ*, 977, 208
- Boquien, M., Burgarella, D., Roehlly, Y., et al. 2019, *A&A*, 622, A103
- Brammer, G. B., van Dokkum, P. G., & Coppi, P. 2008, *The Astrophysical Journal*, 686, 1503
- Bruzual, G., & Charlot, S. 2003, *Monthly Notices of the Royal Astronomical Society*, 344, 1000
- Burgarella, D., Buat, V., & Iglesias-Pramo, J. 2005, *Monthly Notices of the Royal Astronomical Society*, 360, 1413
- Cai, Z.-Y., Lapi, A., Xia, J.-Q., et al. 2013, *ApJ*, 768, 21
- Chabrier, G. 2003, *Publications of the Astronomical Society of the Pacific*, 115, 763
- Charlot, S., & Fall, S. M. 2000, *The Astrophysical Journal*, 539, 718
- da Cunha, E., Charlot, S., & Elbaz, D. 2008, *Monthly Notices of the Royal Astronomical Society*, 388, 1595
- da Cunha, E., Walter, F., Smail, I. R., et al. 2015, *The Astrophysical Journal*, 806, 110
- Davis, M., Guhathakurta, P., Konidaris, N. P., et al. 2007, *The Astrophysical Journal*, 660, L1L6
- Diemer, B. 2018, *ApJS*, 239, 35
- Draine, B. T., Aniano, G., Krause, O., et al. 2014, *The Astrophysical Journal*, 780, 172
- Eales, S., Dunne, L., Clements, D., et al. 2010, *PASP*, 122, 499
- Eisenstein, D. J., Willott, C., Alberts, S., et al. 2023, *arXiv*
- Erb, D. K., Pettini, M., Shapley, A. E., et al. 2010, *ApJ*, 719, 1168
- Euclid Collaboration . 2023, *arXiv*.
<http://arxiv.org/abs/2206.14944>
- Finkelstein, S. L., Dickinson, M., Ferguson, H. C., et al. 2017., *JWST Proposal ID 1345. Cycle 0 Early Release Science*
- Fontana, A., D’Odorico, S., Poli, F., et al. 2000, *The Astronomical Journal*, 120, 2206
- Förster Schreiber, N. M., & Wuyts, S. 2020, *ARA&A*, 58, 661
- Franco, M., Elbaz, D., Bethermin, M., et al. 2018, *A&A*, 620, A152
- Franco, M., Elbaz, D., Zhou, L., et al. 2020, *A&A*, 643, A30
- Fritz, J., Franceschini, A., & Hatziminaoglou, E. 2006, *Monthly Notices of the Royal Astronomical Society*, 366, 767
- Gardner, J. P., Mather, J. C., Clampin, M., et al. 2006, *Space Science Reviews*, 123, 485606
- Giacconi, R., Zirm, A., Wang, J., et al. 2002, *The Astrophysical Journal Supplement Series*, 139, 369
- Giavalisco, M., Ferguson, H. C., Koekemoer, A. M., et al. 2004, *The Astrophysical Journal*, 600, L93
- Gillman, S., Gullberg, B., Brammer, G., et al. 2023, *A&A*, 676, A26
- Granato, G. L., Zotti, G. D., Silva, L., Bressan, A., & Danese, L. 2004, *ApJ*, 600, 580
- Grazian, A., Fontana, A., Santis, C. D., et al. 2006, *A&A*, 449, 951
- Grogin, N. A., Kocevski, D. D., Faber, S. M., et al. 2011, *The Astrophysical Journal Supplement Series*, 197, 35
- Gullberg, B., Smail, I., Swinbank, A. M., et al. 2019, *MNRAS*, 490, 4956
- Guo, Y., Ferguson, H. C., Giavalisco, M., et al. 2013, *The Astrophysical Journal Supplement Series*, 207, 24
- Hainline, L. J., Blain, A. W., Smail, I., et al. 2011, *ApJ*, 740, 96
- Harris, C. R., Millman, K. J., van der Walt, S. J., et al. 2020, *Nature*, 585, 357362
- Hatsukade, B., Kohno, K., Yamaguchi, Y., et al. 2018, *Publications of the Astronomical Society of Japan*, 70, 105
- Hatton, S., Devriendt, J. E. G., Ninin, S., et al. 2003, *Monthly Notices of the Royal Astronomical Society*, 343, 75106

- Hughes, D. H., Serjeant, S., Dunlop, J., et al. 1998, *Nature*, 394, 241
- Hunt, L. K., De Looze, I., Boquien, M., et al. 2019, *Astronomy and Astrophysics*, 621, A51
- Hunter, J. D. 2007, *Computing in Science and Engineering*, 9, 90
- Hnig, S. F., Kishimoto, M., Tristram, K. R. W., et al. 2013, *ApJ*, 771, 87
- Ivezi, ., Kahn, S. M., Tyson, J. A., et al. 2019, *The Astrophysical Journal*, 873, 111
- Jakobsen, P., Ferruit, P., Alves de Oliveira, C., et al. 2022, *Astronomy and Astrophysics*, 661, A80
- Jones, E., Oliphant, T., Peterson, P., et al. 2001,
- Kartaltepe, J. S., Rose, C., Vanderhoof, B. N., et al. 2023, *ApJL*, 946, L15
- Koekemoer, A. M., Faber, S. M., Ferguson, H. C., et al. 2011, *The Astrophysical Journal Supplement Series*, 197, 36
- Laigle, C., McCracken, H. J., Ilbert, O., et al. 2016, *ApJS*, 224, 24
- Lapi, A., Raimundo, S., Aversa, R., et al. 2014, *ApJ*, 782, 69
- Laureijs, R., Amiaux, J., Arduini, S., et al. 2011, *arXiv*
- Lawrence, A., Warren, S. J., Almaini, O., et al. 2007, *Monthly Notices of the Royal Astronomical Society*, 379, 1599
- Leisawitz, D., Hyde, T. T., Rinehart, S. A., & Weiss, M. 2008, in *Society of Photo-Optical Instrumentation Engineers (SPIE) Conference Series*, Vol. 7010, *Space Telescopes and Instrumentation 2008: Optical, Infrared, and Millimeter*, ed. J. M. Oschmann, Jr., M. W. M. de Graauw, & H. A. MacEwen, 701028
- Lelli, F., McGaugh, S. S., & Schombert, J. M. 2016, *AJ*, 152, 157
- Liao, C.-L., Chen, C.-C., Wang, W.-H., et al. 2024, *ApJ*, 961, 226
- Liao, C.-L., Chen, C.-C., Wang, W.-H., et al. 2024, *ApJ*, 961, 226
- Lilly, S. J., Eales, S. A., Gear, W. K. P., et al. 1999, *ApJ*, 518, 641
- Ling, C.-T., Goto, T., Kim, S. J., et al. 2024, <https://arxiv.org/abs/2402.05386>
- Liu, D., Daddi, E., Dickinson, M., et al. 2018, *The Astrophysical Journal*, 853, 172
- Long, A. S., Antwi-Danso, J., Lambrides, E. L., et al. 2024, *The Astrophysical Journal*, 970, 68
- Lower, S., Narayanan, D., Leja, J., et al. 2020, *The Astrophysical Journal*, 904, 33
- Lu, S., Zhu, K., Cappellari, M., et al. 2023, *arXiv e-prints*, arXiv:2304.11712
- Madau, P. 1995, *The Astrophysical Journal*, 441, 18
- Mancuso, C., Lapi, A., Shi, J., et al. 2016, *ApJ*, 833, 152
- Maraston, C. 2005, *Monthly Notices of the Royal Astronomical Society*, 362, 799
- McElwain, M. W., Feinberg, L. D., Perrin, M. D., et al. 2023, *Publications of the Astronomical Society of the Pacific*, 135, 058001
- Merlin, E., Santini, P., Paris, D., et al. 2024, *A&A*, 691, A240
- Michałowski, M. J., Dunlop, J. S., Cirasuolo, M., et al. 2012, *A&A*, 541, A85
- Mitra, D., Negrello, M., DeZotti, G., & Cai, Z.-Y. 2024, *Monthly Notices of the Royal Astronomical Society*, 530, 2292
- Noll, S., Burgarella, D., Giovannoli, E., et al. 2009, *Astronomy and Astrophysics*, 507, 1793
- Pantoni, L., Lapi, A., Massardi, M., et al. 2021, *Monthly Notices of the Royal Astronomical Society*, 504, 928
- Pearson, E. A., Eales, S., Dunne, L., et al. 2013, *Monthly Notices of the Royal Astronomical Society*, 435, 2753
- Pforr, J., Maraston, C., & Tonini, C. 2012, *Monthly Notices of the Royal Astronomical Society*, 422, 3285
- Pforr, J., Maraston, C., & Tonini, C. 2013, *Monthly Notices of the Royal Astronomical Society*, 435, 1389
- Planck Collaboration VI., 2020, *A&A*, 641, A6
- Rieke, M. J., Kelly, D. M., Misselt, K., et al. 2023, *Publications of the Astronomical Society of the Pacific*, 135, 028001
- Rigby, J., Perrin, M., McElwain, M., et al. 2023, *Publications of the Astronomical Society of the Pacific*, 135, 048001
- Rowlands, K., Dunne, L., Dye, S., et al. 2014, *Monthly Notices of the Royal Astronomical Society*, 441, 1017
- Scoville, N., Aussel, H., Brusa, M., et al. 2007, *The Astrophysical Journal Supplement Series*, 172, 18
- Simpson, J. M., Swinbank, A. M., Smail, I., et al. 2014, *ApJ*, 788, 125
- Simpson, J. M., Smail, I., Swinbank, A. M., et al. 2017, *ApJ*, 839, 58
- Siringo, G., Kreysa, E., Kovcs, A., et al. 2009, *A&A*, 497, 945
- Smail, I., Ivison, R. J., & Blain, A. W. 1997, *The Astrophysical Journal*, 490, L5
- Straatman, C. M. S., Spitler, L. R., Quadri, R. F., et al. 2016, *The Astrophysical Journal*, 830, 51
- Swinbank, A. M., Chapman, S. C., Smail, I., et al. 2006, *MNRAS*, 371, 465
- Swinbank, A. M., Simpson, J. M., Smail, I., et al. 2014, *Monthly Notices of the Royal Astronomical Society*, 438, 1267

- Swinbank, A. M., Harrison, C. M., Trayford, J., et al. 2017, *MNRAS*, 467, 3140
- Tan, Q.-H., Daddi, E., Magnelli, B., et al. 2024, *Nature*, 636, 69
- Thomas, D., Maraston, C., Schawinski, K., Sarzi, M., & Silk, J. 2010, *MNRAS*, 404, 1775
- Toft, S., Smolčić, V., Magnelli, B., et al. 2014, *ApJ*, 782, 68
- Turner, O. J., Cirasuolo, M., Harrison, C. M., et al. 2017, *MNRAS*, 471, 1280
- van der Walt, S., Colbert, S. C., & Varoquaux, G. 2011, *Computing in Science and Engineering*, 13, 2230
- Waskom, M. 2021, *The Journal of Open Source Software*, 6, 3021
- Wiklind, T., Conselice, C. J., Dahlen, T., et al. 2014, *The Astrophysical Journal*, 785, 111
- Williams, C. C., Curtis-Lake, E., Hainline, K. N., et al. 2018, *ApJS*, 236
- Wisnioski, E., Förster Schreiber, N. M., Fossati, M., et al. 2019, *ApJ*, 886, 124
- Yamaguchi, Y., Kohno, K., Hatsukade, B., et al. 2020, *Publications of the Astronomical Society of Japan*, 72
- Yang, Q., Shen, Y., Liu, X., et al. 2020, *ApJ*, 900, 58